Clouds of Beryllium Ions in a Paul Trap with Transparent Electrodes

Master Thesis

Author: Alexander Wilzewski (Student ID: 2706488)
Supervisor: Univ.-Prof. Dr. Dmitry Budker
Co-Supervisor: Univ.-Prof. Dr. Ferdinand Schmidt-Kaler

Department of Physics
FB08 - Faculty of Physics, Mathematics and Computer Science
Johannes Gutenberg-Universität Mainz

April 14, 2020

Eidesstattliche Versicherung

Hiermit versichere ich an Eides statt, dass ich die vorliegende Arbeit selbstständig und ohne die Benutzung anderer als der angegebenen Hilfsmittel angefertigt habe. Alle Stellen, die wörtlich oder sinngemäß aus veröffentlichten und nicht veröffentlichten Schriften entnommen wurden, sind als solche kenntlich gemacht. Die Arbeit ist in gleicher oder ähnlicher Form oder auszugsweise im Rahmen einer anderen Prüfung noch nicht vorgelegt worden. Ich versichere, dass die eingereichte elektronische Fassung der eingereichten Druckfassung vollständig entspricht.

Die Strafbarkeit einer falschen eidesstattlichen Versicherung ist mir bekannt, namentlich die Strafandrohung gemäß § 156 StGB bis zu drei Jahren Freiheitsstrafe oder Geldstrafe bei vorsätzlicher Begehung der Tat bzw. gemäß § 161 Abs. 1 StGB bis zu einem Jahr Freiheitsstrafe oder Geldstrafe bei fahrlässiger Begehung.

A. Wilzewski

Alexander Wilzewski

Mainz, den 14.04.2020

Abstract

In this thesis I present clouds of Beryllium ions that were trapped in a segmented Paul trap. The novelty of the trap design are two quartzglas substrates, on which a gold-electrode structure is lithographically applied on, facing each other. An additional feature is an electrically conducting but optically transparent center electrode consisting of indium-tin-oxide (ITO), that allows fluorescence imaging of the Beryllium ions through the trap substrates, while preventing stray charges from accumulating. This trap was designed as an alternative capture-trap for the GBAR experiment, which aims at measuring the gravitational mass of Antihydrogen in a free-fall experiment. For this, $\bar{\mathrm{H}}^+$-ions of energies of a few eV will be captured and sympathetically cooled within a large $^9\mathrm{Be}^+$-ion crystal close to the Doppler cooling limit of $^9\mathrm{Be}^+$ at 0.47 mK. Subsequently, they will be transferred to the so-called precision trap for further cooling. The feasibility and efficiency of sympathetic cooling of the nine-times lighter $\bar{\mathrm{H}}^+$-ion compared to $^9\mathrm{Be}^+$ will be investigated with p^+ mimicking the $\bar{\mathrm{H}}^+$-ions. Since the design is based on atom-chip technology, it is also of interest for the antimatter-on-a-chip (AMOC) project with the goal of developing an efficient way of recombining positrons and antiprotons to form cold antihydrogen, that is then stored in an on-chip magnetic trap for further experiments. During this work the trap components were assembled and integrated in a vacuum chamber. I assembled the optical systems necessary for efficient photoionization of Beryllium atoms and Doppler cooling of their corresponding ions were set up. The ion clouds were trapped for about 100 ms). Numerical simulations of the electric potential open the possibility for further optimization of the trap setup and enhance the trapping times.

Zusammenfassung

Für die vorliegende Arbeit wurden von mir Wolken von Beryllium Ionen in einer segmentierten Paulfalle gefangen. Die Neuheit im Aufbau der hier verwendenten Falle besteht darin, dass sich ihre aus Gold bestehende Elektrodengeomertrie auf zwei Quartzglsssubstraten befindet, welche sich gegenüberliegen. Zusätzlich sind die Radiofrequenzelektroden in der Mitte durch eine optisch transparenten aber elektrisch leitende Schicht aus Idiumzinnoxid getrennt, welche es erlaubt das Fluoreszenzlicht der Ionen durch die Fallenstruktur selbst zu beobachten, es aber gleichzeitig verhindert, dass sich Streuladungen ansammeln. Diese Falle ist eine mögliche Version der "capture-trap" im GBAR-Experiment am CERN, welches das Ziel hat die schwere Masse von Antiwasserstoff in einem Freifallexperiment zu messen. Dazu sollen $\bar{\mathrm{H}}^{+}$-Ionen mit Energien von ein paar Elektronenvolt in einem großen Kristall aus Beryllium Ionen eingefangen und in diesem sympthetisch gekühlt werden. Darauf werden die $\bar{\mathrm{H}}^{+}$-Ionen, die sich nun bei Temperaturen nahe des Dopplerkühllimits für $^{9}\mathrm{Be}^{+}$ von 0.47 mK befinden, in die sogenannte "precision-trap" transportiert und dort weiter, in den µK Bereich, weiter runtergekühlt. Die Effizienz des sympathetischen Kühlens mit dem unvorteilhaften Massenverhältnis von 9:1 wird mit Protonen, welche praktisch dasselabe Masse-zu-Ladung Verhältnis haben wie $\bar{\mathrm{H}}^{+}$, getestet. Da die hier verwendete Falle auf Technologien basiert die Anwendung in Atomchipexperimenten findet, ist die Untersuchung derselbigen auch relevant für das "antimatter-on-a-chip" (AMOC)-Projekt, welche das Ziel verfolgt Antiprotonen und Positronen effizient zur Rekombination zu bringen um kalten Antiwasserstoff in größeren Mengen zu produzieren. Für die vorliegende Arbeit wurde die Falle zusammengebaut und in eine entsprechende Vakuumkammer integriert. Desweiteren habe ich die notwendigen optischen Systeme für eine effiziente Photoionisation von Berylliumatomen und das Dopplerkühlen der entsprechenden Ionen aufgebaut. Die gezeigten Ionenwolken konnten für etwa 100 ms in der Falle gespeichert werden. Außerdem wurde das elektrische Potential innerhalb der Fallenstruktur numerisch simuliert, was zukünftige Optimierung ermöglicht sowie dabei helfen wird die Speicherzeiten der Ionen zu verlängern.

Contents

List of Figures

List of Tables

1 Introduction: Fundamental Research on Antimatter

Paul Dirac predicted the existence of an anti-electron in his effort to find a relativistic version of the Schrödinger equation in 1928 [Dirac 1928]. Four years later, in 1932, Carl Anderson experimentally discovered the positively charged counterpart of the electron [Anderson 1933]. This discovery marks the starting point of an era of discovering new particles and their antimatter counterparts. For example, negatively and positively charged muons and pions formed in cosmic ray interactions were observed in cloud chambers, roughly a decade later. Research on antimatter also sparked development and construction of particle accelerators like the Bevatron at the Lawrence Berkeley National Laboratory reaching sufficiently high energies to form anti-protons in collisions, which were shown to exist by Emilio Segrè and Owen Chamberlain in 1955 [Chamberlain et al. 1955]. The efforts to find the most general theory that explains the vast amount of particles and their interactions measured over the years, culminated in the Standard Model of particle physics. With the discovery of the Higgs boson [ATLAS-Collaboration et al. 2012] the Standard Model has correctly predicted the outcome of any high energy experiment so far. Despite its great success, it is to this day unable to explain significant observations. One of the most prominent open questions in physics of today, which the current theoretical framework is unable to account for, is why the visible mass of the the universe seems to consist only of matter and not antimatter [Dine and Kusenko 2004; Canetti, Drewes, and Shaposhnikov 2012]. As a consequence of the CPT theorem, the invariance under simultaneous Charge, Parity and Time inversion, matter and antimatter should show the same behaviour, apart from having opposite charge, in all situations [Eades and Hartmann 1999]. Many experiments, most of them situated at the antiproton decelerator (AD) facility at CERN, are dedicated to confirm the predictions of the CPT theorem by comparing fundamental properties of antimatter to those of their matter counterparts. The BASE collaboration measured the antiprotons magnetic moment with a precision of one part per billion and showed that at that level of precision has the same value as the protons magnetic moment [Smorra et al. 2017]. he comparison of the charge-to-mass ratios of protons and antiprotons with a sub-ppb precision by measuring their cyclotron frequencies in a Penning trap [Gabrielse et al. 1999] was another test of CPT symmetry. This experiment confirms that the equivalence of the inertial masses m_i of antiprotons and protons within the precision of the measurement. However, an open question is whether the gravitational masses m_g, the masses that couple them to an external gravitational field, are the same. According to Einstein's *weak equiva-*

lence principle (WEP) in general relativity they should indeed be equivalent. On the other hand, a deviation could lead to a possible explanation of the observed matter-antimatter asymmetry in the universe. The only experimental limits on the gravitational mass of antimatter were published by the ALPHA collaboration [Amole et al. 2013]. In this experiment antihydrogen was released from a magnetic bottle and by reconstruction of the annihilation vertices on the boundaries of the trap, they were able to constrain the ratio of the gravitational masses of hydrogen and antihydrogen by $-110 < m_g(\bar{\mathrm{H}})/m_g(\mathrm{H}) < 75$. Even though these is the first direct measurement of the gravitational mass of antimatter, not even determining the sign of the $m_g(\bar{\mathrm{H}})$ is insufficient to exclude or put reasonable limits on any modified theory of gravitation for antimatter. The ALPHA experiment suffers not only from high initial velocities of the Antihydrogen, but also the systematic errors caused by the magnetic fields, inevitable in order to trap the neutral antihydrogen atoms, have to be well understood and accounted for since they spoil any gravitational force to a large degree.

GBAR

There are several experiments aiming for an improved measurement of the gravitational mass of antimatter. The GBAR experiment was proposed by Jochen Walz and Theodor Hänsch [Walz and Hänsch 2004] in 2004, and was founded in 2011[Pérez 2011] and then approved by CERN. The idea of GBAR is to perform a free-fall experiment of ultracold antihydrogen atoms in the gravitational field of the earth. The ultracold regime will be reached by utilizing cooling schemes that are well established in the atomic physics and trapped ion community. Direct laser cooling on the Lyman-α transition with a natural line width of $\Gamma \approx 2\pi \cdot 100\,\mathrm{MHz}$ does result in a Doppler cooling limit of $2.4\,\mathrm{mK}$ [Setija et al. 1993], equivalent to a mean velocity of $7\,\mathrm{m\,s^{-1}}$. This not sufficient to reach the anticipated precision of the gravitational mass measurement in GBAR, where simulations show [Wolf 2019] that a temperature of $T \approx 5\,\mu\mathrm{K}$ is required to reach a relative precision on the percent level within two weeks of measurement. Thus the approach of sympathetic cooling of in a Paul trap is chosen.

In the last stage of the experiment a Coulomb crystal consisting of a single Antihydrogen ion $\bar{\mathrm{H}}^+$ and an optically accessible Beryllium ion will be cooled close to the motional ground state of the trapping potential, before the excess positron will be photo-detached and the now no more confined neutral antiatom will fall down (or up) and annihilate. This will happen in the so-called precision trap, that was already characterized and in which a test ion crystal of one Calcium ion $^{40}\mathrm{Ca}^+$ and one Beryllium ion $^{9}\mathrm{Be}^+$ were cooled well below the Doppler cooling limit [Wolf 2019] by employing sideband cooling. Sympathetic cooling becomes increasingly inefficient for larger mass ratio of the constituent ions of the crystal [Kielpinski et al. 2000; Wübbena et al. 2012]. Therefore, going from the $^{40}Ca^{+}$-$^{9}Be^{+}$ ion crystal with a mass ratio of $\approx$ 4:1, to the desired $^{9}Be^{+}$-$\bar{H}^{+}$ with 9:1 mass ratio is challenging and requires already cold $\bar{H}^{+}$ ions. It is expected that only a few antihydrogen ions at a center energy of keV and a temperature of 10 eV are created for each antiproton bunch coming from the ELENA ring every 110 s. Five meters behind the production chamber of the antihydrogen ions, where the precsion trap and the free-fall chamber will be located, this results in spatial spread of a few centimeters, so that the micron-sized electrode structure of the precision trap cannot efficiently capture the ions. The solution to this problem will be a second trap in front of the precision trap, with appropriate dimensions where the $\bar{H}^{+}$-ions will be captured and sympathetically pre-cooled close to the Doppler cooling limit in a large Beryllium ion crystal ($\approx 10^5$ ions), and then transported to the precision trap. It the assembly and first testing of a possible design of this capture-trap based on atom-chip technology [Folman et al. 2002] that is the central subject presented in this work.

AMOC

This capture trap is also of interest for the antimatter-on-a-chip (AMOC) project, currently at the proposal stage, with the goal of designing a chip-based trap to efficiently recombine antiprotons and positrons to form antihydrogen and keep it place. The idea is based on a preliminary numerical investigation, that shows that, it is in principle possible to confine particles with very different charge-to-mass ratios in the same volume of a Paul trap [Leefer et al. 2017] and in such a way significantly increase the production rate of $\bar{H}$. Having a larger amount of antihydrogen available opens up the possibility to improve current experiments, not only (anti)gravity, but also other CPT tests, like they are performed by the ALPHA collaboration with the spectroscopy on the 1S $\leftrightarrow$ 2S [Ahmadi et al. 2018a] and 1S $\leftrightarrow$ 2P transition [Ahmadi et al. 2018b] and, just recently published, the measurement of the Lamb shift [Ahmadi, Alves, et al. 2020] in antihydrogen. Also for AMOC, the aim is to eventually capture and cool antiprotons and establishing cooling techniques, like sympathetic cooling of ions with very disadvantages mass ratios of 9:1, are essential.

2 Relevant Theory

In this chapter the theoretical basis necessary for understanding and description of the experiment and its goals is reviewed. In the first part, the general idea of Paul traps and how to describe charged particles in such traps is outlined. In the second part will focus on the concept of laser cooling and how it is relevant for this work with Beryllium ions.

2.1 Paul Traps

Confining charged particles in an electric field is not as straight forward as one might think. From the Laplace equation in a charge-free space

$$\Delta\Phi(x, y, z, t) = 0 \tag{1}$$

one can conclude that at any point in time and space the electric potential $\Phi(x, y, z, t)$ cannot take on a minimum in all three spatial dimensions. Another way to look at this is by considering the equivalent statement $\nabla\vec{E} = 0$, meaning that equal amounts of electric field lines have to flow into and out of each point, meaning that there is always an "escape path" for the particles. The ground-breaking idea of Wolfgang Paul, first published in [Paul, Reinhard, and Zahn 1958], was to use a dynamic way of confinement, relying on oscillating fields at radio-frequencies (RF) that made it possible to create a net-restoring pondero-motive force in all directions.

In order to understand the concept of such RF traps an electric potential with a depth of Φ_0 at a distance r_0 and a quadrupolar shape is considered [Dehmelt 1969]:

$$\Phi(x, y, z) = \frac{\Phi_0}{2r_0^2} \cdot (\alpha x^2 + \beta y^2 + \gamma z^2). \tag{2}$$

Eq.(1) imposes the condition

$$\alpha + \beta + \gamma = 0 \tag{3}$$

on the geometric factors α, β, γ. This is, for example, satisfied by choosing $\alpha = \beta = 1, \gamma = -2$, which would describe an electrode configuration as shown in Fig. 1(a), where r_0 is the radius of the ring electrode and $\sqrt{2}z_0 = r_0$.

Another simple choice is $\alpha = -\beta = 1, \gamma = 0$ describing the potential between the electrodes shown in Fig.1(b), which will lead to confinement in the xy-plane, and we will have a closer look at this choice for a first understanding of the working principle of Paul traps.

Confinement in Two Dimensions

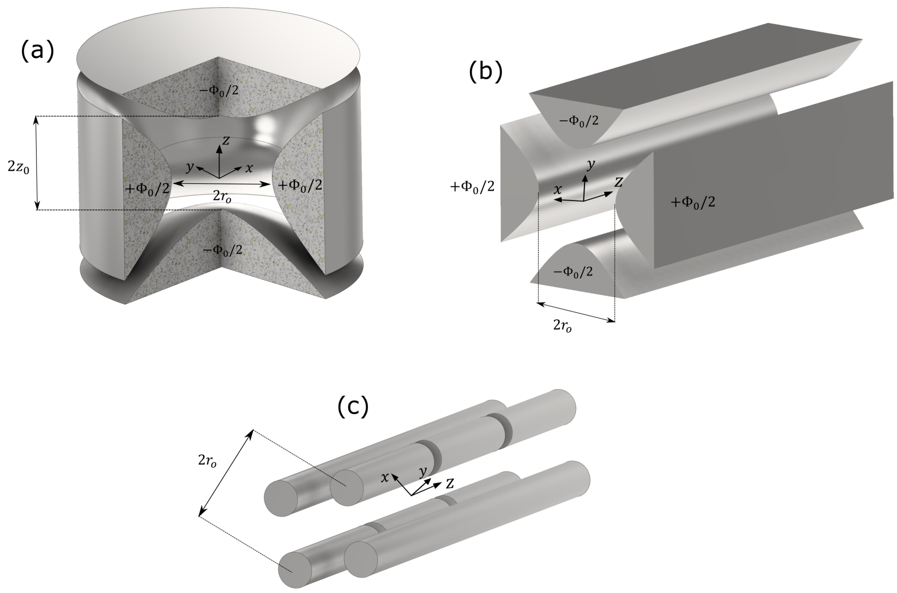

Figure 1: Different realizations of RF traps: (a) Ring electrode trap with hyperbolically shaped electrodes; (b) Quadrupole mass filter; (c) Segmented linear Paul trap. Applying a constant voltage on the outer four segments will result in axial confinement, while a RF field on the other pair of electrodes will provide radial confinement.

When we apply a voltage Φ_0 between the electrode pairs in Fig. 1(b), the electric field inside the electrode structure is given by

$$\vec{E} = -\nabla \cdot \Phi = -\nabla \cdot \frac{\Phi_0}{2r_0^2} \cdot (x^2 - y^2) = \frac{\Phi_0}{r_0^2} \cdot \begin{pmatrix} -x \\ y \\ 0 \end{pmatrix}. \tag{4}$$

From this one can see, that if Φ_0 is constant in time and we would place a charged particle between the electrodes, it would be held into place in one direction, while accelerating towards the other and eventually collide with them. Thus we will apply a periodic voltage, composed of a static part U_0 and time-dependent part with of amplitude V_0 and radio-frequency (RF) Ω_{RF}, typically tens of Megahertz for ions,

$$\Phi_0 = U_0 + V_0 \cos(\Omega_{RF} t). \tag{5}$$

The motion of a particle with mass m and charge Q is then classically described

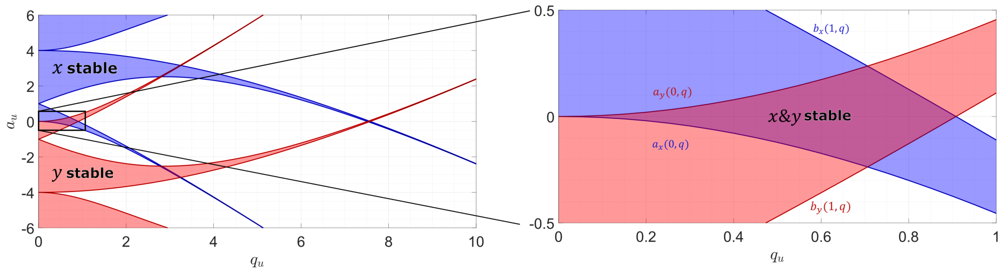

Figure 2: Stability diagram for Mathieu equations in two dimensions, stable solutions for the ion trajectory are only possible in the the overlapping region. The first stable region at the origin is zoomed in on the right side.

by

$$\begin{aligned}\ddot{x} + \frac{Q}{mr_0^2}[U_0 + V_0\cos(\Omega_{RF}t)]x = 0,\\ \ddot{y} - \frac{Q}{mr_0^2}[U_0 + V_0\cos(\Omega_{RF}t)]y = 0.\end{aligned} \tag{6}$$

One might think that that the oscillating part would average out and that there would be no net force in the time average. This is true for a homogeneous field, but for an inhomgeneous field, like the quadrupol, there will be a ponderomotive force towards the point of lowest field amplitude. Similar effects can also be observed for other forces than the electromagnetic force, for example, when a standing sound wave build up inside a tube, dust particles will accumulate at the nodes of the wave. Let us quantify this further by substituting

$$\begin{aligned} a_x = -a_y &= \frac{4QU_0}{m\Omega_{RF}^2 r_0^2},\\ q_x = -q_y &= \frac{2QV_0}{m\Omega_{RF}^2 r_0^2},\\ \tau &= \frac{\Omega_{RF}t}{2}\end{aligned} \tag{7}$$

into Eq.(6) and obtaining

$$\frac{d^2u}{d\tau^2} + [a_u + 2q_u\cos(2\tau)]u = 0, \qquad u = (x, y). \tag{8}$$

In mathematics differential equations of this form are known as Mathieu's equations and are well studied. Floquet's theorem tells us that there are two linearly independent solutions of these equations, of which at least one is guaranteed to be periodic. The general solutions can be divided into stable and unstable solutions depending on whether the trajectory of the particle is bound to a specific volume for all times or diverges as $\tau \to \infty$. The stability of the solution is

only determined by the the values of a_u and q_u, which are therefor also known as stability parameters. This suggests the division of the (a_u, q_u)-plane into a stable and unstable region [Paul, Reinhard, and Zahn 1958; Major, Gheorghe, and Werth 2005], shown in Fig.2. The shaded regions are stable since here both solutions of Mathieu's equationa are periodic. In the white areas, one of the solutions contains an exponentially growing factor and thus is unstable. On the characteristic curves separating the two regions, the two solutions contain factors oscillating with an integer-multiple of the driving frequency Ω_{RF} and one of them grows linearly for $\tau \to \infty$. A physical interpretation for this is that driving field actually resonantly excites the motion of the particles in the trap.
By using $a_x = -a_y$ and $q_x = -q_y$ we obtain the composite plot for both direction shown in Fig. 2 and a stable confinement in both directions is given when these regions overlap. Paul traps are usually operated in the first stability region at the origin, zoomed in on the right-hand side of Fig. 2. If the particle motion is stable, its trajectory can be expanded into a Fourier series

$$u(\tau) = A_u \sum_{n=-\infty}^{\infty} c_{2n} \cos[(\beta_u + 2n)\tau] + B_u \sum_{n=-\infty}^{\infty} c_{2n} \sin[(\beta_u + 2n)\tau]. \tag{9}$$

The initial conditions of the particle enter in the form of the coefficients A_u and B_u and the parameter β_u is a function of the stability parameters a_u, q_u. It can be obtained by a recursive fractional expression from which also the Fourier coefficients c_{2n} are determined [Major, Gheorghe, and Werth 2005]. In practice traps are at $a_u, q_u \ll 1$ and $\beta_u^2 \approx a + \frac{q_u^2}{2}$. In that case also the Fourier coefficients rapidly decrease and in good approxiamtion terminate after $|n| > 1$ and $c_{\pm 2} = -\frac{q_u}{4} c_0$. Together with the initial coniditon $B_u = 0$ we can then rewrite Eq.(9) in the lowest-order approximation

$$u(t) = A_u c_0 \cos(\beta_u \frac{\Omega_{RF}}{2} t) \left[1 - \frac{q_u}{2} \cos(\Omega_{RF} t)\right]. \tag{10}$$

One can see that the ions trajectory is composed of a slowly oscillating term at $\omega_{u,0} = \beta_u \frac{\Omega_{RF}}{2}$ known as *secular motion* and a fast oscillation at the driving frequency, the so-called *micromotion*.

Pseudopotential Approximation

In Eq.(10) the amplitude of the micromotion is reduced by a factor of $q_u/2$ compared the secular motion and thus the ion's trajectory can be pictured as a smooth secular motion $\mathcal{S}$ with the micromotion $\mathcal{M}$ being a fast and small perturbation to it [Wuerker, Shelton, and Langmuir 1959]:

$$x(t) = \mathcal{S}(t) + \mathcal{M}(\mathcal{S}, t), \tag{11}$$

where for now only the x-dimension is considered. One can further separate the electric potential into a static component $\Phi_{\mathcal{S}}(x)$ governing the secular motion and a time-dependent component $\Phi_{\mathcal{M}}(x,t)$ being responsible for the micromotion. The forces on the particle are then given by

$$F(x) = -Q\,\partial_x \Phi_{\mathcal{S}}(x) \tag{12a}$$

$$f(x,t) = -Q\,\partial_x \Phi_{\mathcal{M}}(x,t) = f_0(x)\cos(\Omega_{RF} t), \tag{12b}$$

with $f_0(x) = -\frac{QV_0}{r_0^2}x$. If the variation in the field amplitude is small over one cycle of micromotion, the equation of motion can be expanded to first order in $\mathcal{M}$:

$$m\ddot{\mathcal{S}} + m\ddot{\mathcal{M}} = F(\mathcal{S}) + f(\mathcal{S},t) + \mathcal{M}\partial_x(F(x) + f(x,t))|_{\mathcal{S}} + \mathcal{O}(\mathcal{M}^2). \tag{13}$$

Since in this approximation the micromotion is mainly governed by the force $f(\mathcal{S},t)$, it can be separated out from Eq.(13), yielding

$$m\ddot{\mathcal{M}}(\mathcal{S},t) = f(\mathcal{S},t). \tag{14}$$

Inserting Eq.(12b) here, allows to readily solve this equation:

$$\mathcal{M}(\mathcal{S},t) = -\frac{f_0(\mathcal{S})}{m\Omega_{RF}^2}\cos(\Omega_{RF} t). \tag{15}$$

Reinserting the above equation into into Eq.(13) and averaging over one period of micromotion, so that the terms oscillating at Ω_{RF} drop out, leaves:

$$m\ddot{\mathcal{S}} = F(\mathcal{S}) + \frac{1}{T}\int_0^T dt\,\mathcal{M}\cdot\partial_x f(x,t)|_{\mathcal{S}} = F(\mathcal{S}) - \frac{1}{2m\Omega_{RF}^2}(f_0(x)\cdot\partial_x f_0(x))|_{\mathcal{S}}, \tag{16}$$

which is equivalent to

$$m\ddot{\mathcal{S}} = -\partial_x\left(Q\,\Phi_{\mathcal{S}}(x) + \frac{Q^2}{4m\Omega_{RF}^2}(\partial_x\Phi_{\mathcal{M}}(x))^2\right). \tag{17}$$

The main conclusion to draw from this quite lengthy derivation is that the term in the parenthesis in Eq.(17) is a potential energy governing secular. The second term is called *pseudopotential*. The derivation is the same for the other spatial dimensions and we can readily obtain the general form of the potential by replacing $\partial_x \to \nabla$. Thus the pseudopotential will have, in contrast to an actual electric potential, a minimum due to the time-averaging and results in confinement of the particles. The total secular potential is then given by

$$\Phi_{sec} = \Phi_{pseudo}(x, y) + \Phi_{\mathcal{S}}(x, y) = \frac{Q^2 V_0^2}{4m\Omega_{RF}^2 r_0^4}(x^2 + y^2) + \frac{QU_0}{2r_0^2}(x^2 - y^2). \qquad (18)$$

This also lets us estimate the potential depth at the position of the electrodes $x = r_0$ and $y = r_0$:

$$\Phi_{depth} = \frac{Q^2 V_0^2}{4m\Omega_{RF}^2 r_0^2} \pm \frac{QU_0}{2r_0}. \qquad (19)$$

Real Paul Traps

The possibility to trap particles is not limited to hyperbolically shaped electrodes as in Fig. 1(a) and (b), but any electrode configuration that will result in a potential that can be expanded around a point to the quadrupolar form in Eq.(2) is in principle capable of trapping particles. However, the extend to which the potential can be approximated to be quadrupolar and hence the volume in which the above description is valid heavily depends on the actual electrode structure and can be considerably smaller compared to a trap of same dimensions with hyperbolic electrodes. For instance, in Fig. 1(c) a linear Paul is schematically shown, which consists of a quadrupole mass filter with one pair of segmented cylindrical electrodes [Paul 1990]. The geometry of the trap operated in this work is adopted from linear Paul traps. Applying a constant voltage U_{ax} to the outer DC-segments will confine the ions along the trap axis, while radial confinement is provided by the RF field. Around the center of the trap the static component of potential has the form

$$\Phi_{\text{ax}}(x, y, z) = \frac{U_{\text{ax}}}{2r_{0,\text{ax}}^2}[z^2 - \frac{1}{2}(x^2 + y^2)]. \qquad (20)$$

Here the unavoidable consequence of anti-confinement in the radial direction is visible, which counteracts the confining pseudopotential component in Eq.(18). This will become important in the next chapter, when we will simulate the potential in our trap in order to estimate these trap characteristics.

Trap Frequencies

Combining Eq.(18) and Eq.(20) yields the total potential

$$\begin{aligned}\Phi_{\text{total}} = & \left(\frac{Q^2 V_0^2}{4m\Omega_{RF}^2 r_0^4} + \frac{QU_0}{2r_0^2} - \frac{1}{2}\frac{U_{\text{ax}}}{2r_{0,\text{ax}}^2}\right) x^2 \\ & + \left(\frac{Q^2 V_0^2}{4m\Omega_{RF}^2 r_0^4} - \frac{QU_0}{2r_0^2} - \frac{1}{2}\frac{U_{\text{ax}}}{2r_{0,\text{ax}}^2}\right) y^2 \\ & + \frac{U_{\text{ax}}}{2r_{0,\text{ax}}^2} z^2.\end{aligned} \tag{21}$$

By introducing the trap frequencies

$$\begin{aligned}\omega_x^2 &= \frac{Q^2 V_0^2}{2m^2\Omega_{RF}^2 r_0^4} + \frac{QU_0}{mr_0^2} - \frac{QU_{\text{ax}}}{2mr_{0,\text{ax}}^2}, \\ \omega_y^2 &= \frac{Q^2 V_0^2}{2m^2\Omega_{RF}^2 r_0^4} - \frac{QU_0}{mr_0^2} - \frac{QU_{\text{ax}}}{2mr_{0,\text{ax}}^2}, \\ \omega_z^2 &= \frac{QU_{\text{ax}}}{mr_{0,\text{ax}}^2},\end{aligned} \tag{22}$$

Eq.(21) can be re-expressed in the common form of a harmonic potential

$$\Phi_{\text{total}} = \frac{1}{2}m\omega_x^2 x^2 + \frac{1}{2}m\omega_y^2 y^2 + \frac{1}{2}m\omega_z^2 z^2, \tag{23}$$

where the ions perform secular harmonic oscillation in the trapping potential at the frequencies ω_i along the respective axes.

2.2 Beryllium Ion Energy Levels and Doppler Cooling

As outlined in Ch.1, we eventually want to sympathetically cool ions of atomic mass equal to one, for now protons, in a large $^9\text{Be}^+$ Coulomb crystal. In order to reach temperatures of mK and even below, the $^9\text{Be}^+$ ions need to be laser-cooled. Since the first demonstrations of Doppler-cooling [Hänsch and Schawlow 1975; Wineland, Drullinger, and Walls 1978], it is now widely used and we will review the basic ideas and description of it in the following.

Doppler Shift and Broadening

Since the melting point of Beryllium at 1287 °C is quite high, the trap is loaded with Beryllium coming from an atomic oven at about 1000 K. It is possible to estimate the probability for a Beryllium atom at temperature T to have a velocity

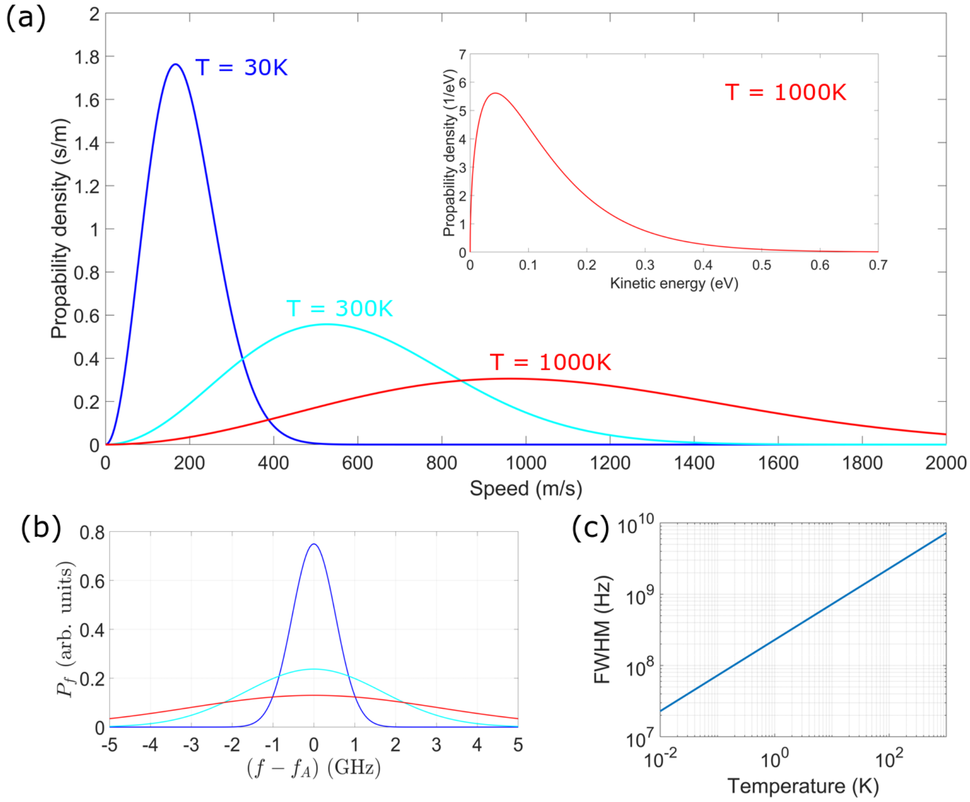

Figure 3: (a) Maxwell-Boltzmann distribution for particles with masses of 9 u at different temperatures. In the inset the 1000 K case is converted to a energy distribution; (b) Relative Doppler broadening of an atomic transition at the same temperatures as in (a); (c) FWHM of the transition as a function of temperature.

v with help of the Maxwell-Boltzmann distribution

$$p(v)dv = 4\pi \left(\frac{m}{2\pi k_B T}^{3/2} \right) v^2 \exp\left(-\frac{mv^2}{2k_B T} \right) dv, \tag{24}$$

with k_B the Boltzmann constant and the mass of Beryllium $m = 9\,\mathrm{u}$. Fig. 3(a) shows this distribution for different temperatures. By imposing $p(v)dv = p(E)dE$ Eq.(24) can be converted to a kinetic energy distribution

$$p(E)dE = 2\sqrt{\frac{E}{\pi}} \left(\frac{1}{k_B T} \right)^{3/2} \exp\left(-\frac{E}{k_B T} \right) dE, \tag{25}$$

which is shown in the inset in Fig. 3(a). This is useful to estimate the fraction of ions that can be trapped for a given trap depth coming from a thermal source, for instance, in our case to be able to trap all ions reaching the trap, it has to be 0.6 eV deep.

By shining a laser, which we model as a classical monochromatic plane wave

$$\vec{E_L}(\vec{x}, t) = \vec{E}_0 \cos(\vec{k_L} \cdot \vec{x} - \omega_L t), \tag{26}$$

with amplitude $\vec{E}_0$ and frequency ω_L, onto the atoms, they will see a Doppler shifted laser frequency ω due to their velocity $\vec{v}$ relative to the wavevector $\vec{k_L}$ of the laser beam:

$$\omega \approx \omega_L \left(1 - \frac{\vec{k_L} \cdot \vec{v}}{|\vec{k_L}|c}\right), \tag{27}$$

in the limit of $v \ll c$. In our experiment the laser beam with wavelength $\lambda = {}^{2\pi c}/_{\omega_L} = 313\,\mathrm{nm}$ is counter-propagating to the atom beam coming from the oven, which corresponds to a relative Doppler shift of $\approx 3\,\mathrm{GHz}$ into the blue at the center velocity of the Maxwell-Boltzmann distribution. Furthermore, if the velocity is isotropically distributed for a gas of atoms or trapped ions the different velocity classes will experience different shifts, which will Doppler broaden the observed absorption- and emission line of an atomic transition at frequency f_A. The observed line is then a convolution of the natural Lorentzian line shape and the Gaussian-shaped velocity distribution, the so-called Voigt-profile. For high temperatures, in our case $> 0.1\,\mathrm{K}$, the Doppler-broadened line width is at least an order of magnitude larger than the natural line width and the resulting spectrum has a Gaussian shape:

$$P_f(f)df = \sqrt{\frac{mc^2}{2\pi k_B T f_A^2}} \exp\left(-\frac{mc^2(f - f_A)^2}{2k_B T f_A^2}\right) df. \tag{28}$$

These lines are shown in Fig. 3(b) for Beryllium at the same temperatures as in Fig. 3(a). In Fig. 3(c) the full-width at half-maximum as function of temperature is plotted, which we can read off Eq.(28):

$$\Delta_{\mathrm{FWHM}} = \sqrt{\frac{8k_B T \ln 2}{mc^2}} f_A. \tag{29}$$

Laser Cooling

The basic idea of laser cooling, illustrated in Fig. 4, is that, for laser light red-detuned by $\delta = \omega_L - \omega_A$ from the atomic resonance $\omega_A = 2\pi f_A$, the light will become resonant when the atom is moving towards laser beam. Hence the more photons are absorbed and re-emitted by the atom the larger the projection of the atoms velocity onto the (negative) wavevector is. For each absorption of a photon the momentum of the atom will change by $\hbar\vec{k}_L$ in the direction of the laser beam and after emission again by $\hbar\vec{k}_{\mathrm{iso}}$ in a random direction. After many absorption-emission cycles the recoils by the isotropic re-emission will average out, and as a net result the kinetic energy of the atom and its translational temperature is

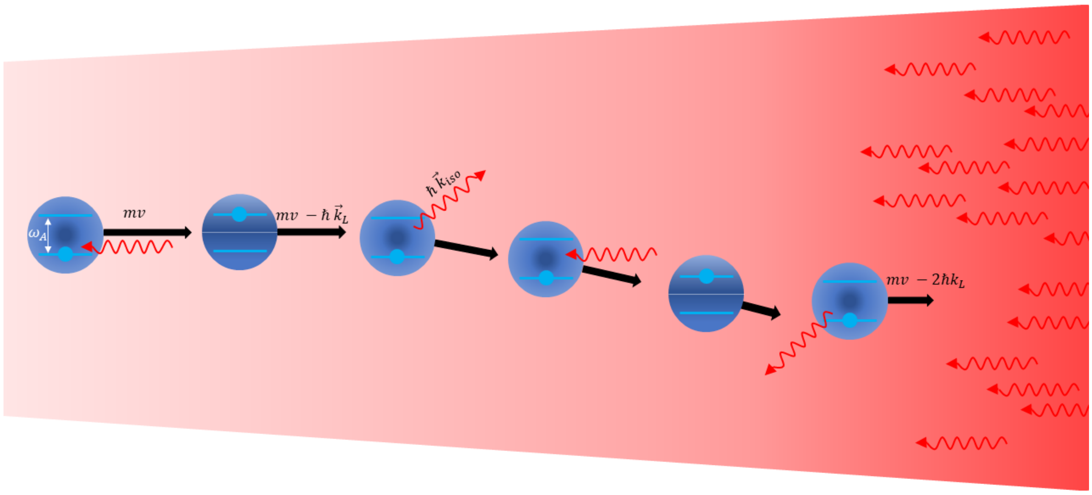

Figure 4: A sketch illustrating the concept of laser cooling. From left to right: By absorbing a photon from a red-detuned laser, the atom's momentum is reduced. Then it gains momentum in a random direction from recoil after spontaneously emitting a photon. As this process continues the isotropic emission averages out and as a net result the momentum of the atom towards the laser is reduced.

reduced. In principle, if one wants to isotropically cool down a gas of atoms, one has to shine a laser from each spatial direction. But since the ions are already trapped and perform harmonic oscillations fixed by the trap geometry, it suffices to align one the laser beam in a direction that has a non-zero projection on all of these oscillation modes.

In a more quantitative way, if one models the atom as a two-level system, the radiation force experienced by the atom can be expressed as [Cohen-Tannoudji 1992]

$$\vec{F}(\vec{v}) = \hbar\vec{k}_L\Gamma_{\mathrm{sc}} = \hbar\vec{k}_L\frac{\Gamma}{2}\frac{\Omega_R^2/2}{(\delta - \vec{k}_L\cdot\vec{v})^2 + (\Gamma^2/4) + (\Omega_R^2/2)}. \tag{30}$$

In Eq.(30), Γ is the natural line width, Γ_{sc} is the scattering rate and Ω_R is the Rabi-frequency of the atomic transition in the laser field. The assumption that the atom and the laser beam are counter-propagating in z-direction allows to express $\vec{k}_L \cdot \vec{v} = -vk_L$ and then taylor Eq.(30) around $v = 0$:

$$F_z(v) = F_z(v=0) - \alpha v + ..., \tag{31}$$

where the term to first order in v acts as a friction force with friction coefficient α. Expanding in powers of $k_L v/\Gamma$ we obtain the following expression for the friction coefficient:

$$\alpha = -\hbar k_L^2 \frac{s}{(1+s)^2}\frac{\delta\,\Gamma}{\delta^2 + (\Gamma^2/4)}, \tag{32}$$

where $s = \frac{\Omega_R^2/2}{\delta^2+(\Gamma^2/4)}$ is the so-called saturation parameter. A red-detuned laser, $\delta < 0$, results in a dissipative friction term $\alpha > 0$. One finds the maximum friction by first noting that for a given value of s Eq.(32) maximizes for $\delta = -\Gamma/2$, and the resulting expression is in turn maximized for $s = 1$ meaning $\Omega_R = \Gamma$, which is achieved by tuning the laser intensity appropriately. This yields

$$\alpha_{\max} = \frac{\hbar k_L^2}{4} = \frac{E_R \cdot m}{2\hbar}, \tag{33}$$

where $E_R = (\hbar k_L)^2/(2m)$ is the recoil energy the atom gains by emitting one photon. For Beryllium ions the maximum friction coefficients takes on the value $10^{-20}\,\mathrm{kg\,s^{-1}}$.
Finally, a lower bound for the temperatures that are achievable with this method has to be found. In order to do so, one has to model heating and cooling with corresponding rates and then find the minimum kinetic energy at thermal equilibrium, where both rates equalize. Note that for trapped ions the zero-order term $F_z(v = 0)$ in Eq.(31) is compensated for by the confining forces of the trap. Thus the re-written equation of motion is

$$m\dot{v} = -\alpha v \tag{34}$$

meaning that the velocity is exponentially damped with $\gamma = \alpha/m$, evaluating to minimum time constant of $\gamma^{-1} = 1.4\,\mu\mathrm{s}$ at maximum friction. Multiplying Eq.(34) by v and rewriting it to

$$\frac{d}{dt}(v^2) = -\alpha v^2 \rightarrow \dot{E}_{kin,cooling} = -\frac{2\alpha}{m} E_{kin} \tag{35}$$

yields an expression for the dissipation of kinetic energy. In a next step, the heating is modelled by considering that for each absorption-emission cycle the atom gains twice the recoil energy E_R, which happens at the scattering introduced in Eq.(30):

$$\dot{E}_{kin,heating} = 2\Gamma_{sc} E_R. \tag{36}$$

When these two rates reach thermal equilibrium we find the residual kinetic energy to be:

$$E_{kin,equi} = \frac{E_R \Gamma_{sc} m}{\alpha}. \tag{37}$$

The above equation takes on a minimum at α_{max}, where $\delta = -\Gamma/2$ and $\Omega_R = \Gamma$ and hence $\Gamma_{sc} = \Gamma/4$, so that one finds

$$E_{kin,equi} = \frac{\hbar\Gamma}{2}, \tag{38}$$

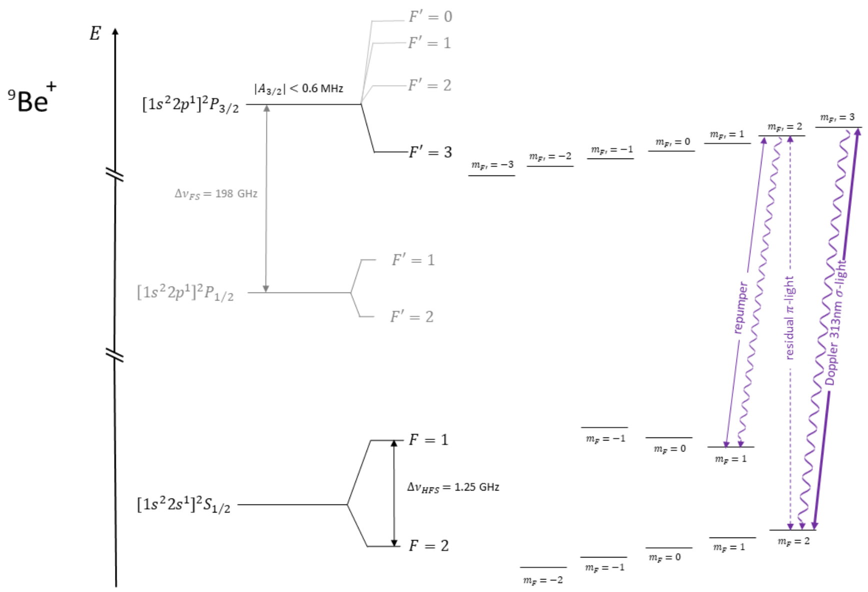

Figure 5: Energy level diagram of $^9\mathrm{Be}^+$. Doppler cooling is performed on the $^2S_{1/2}(F = 2, m_F = 2) \leftrightarrow {}^2P_{3/2}(F' = 3, m_{F'} = 3)$ transition. Further details and explanation can be found in the text.

which is equivalent to a temperature of

$$T_D = \frac{\hbar\Gamma}{2k_B}, \tag{39}$$

known as the Doppler cooling limit, which amounts to 0.47 mK for Beryllium ions.

Beryllium Ion Energy Levels

Beryllium is an alkaline earth metals in the second main group of the periodic table. Their corresponding ions have on one electron in their outer shell turning them into hydrogen-like systems. For efficient Doppler cooling, a transition with a large electric dipole moment is desired and for $^9\mathrm{Be}^+$ this is the $^2S_{1/2} \leftrightarrow {}^2P_{3/2}$ transition at a frequency of $\omega_A = 2\pi \cdot 957\,396\,616.6$ MHz and a natural line width $\Gamma = 2\pi \cdot 19.64$ MHz [Nörtershäuser et al. 2015]. The relevant energy level diagram is shown in Fig. 5. Since Beryllium has a nuclear spin $I = -3/2$, the $^2S_{1/2}$ ground state has two and the $^2P_{3/2}$ excited state has four hyperfine levels. The hyperfine splitting of the $F = 1$ and $F = 2$ ground-state is 1.25 GHz and the hyperfine constant of the $^2P_{3/2}$ is known to be $|A_{3/2}| < 0.6$ MHz [Poulsen, Andersen, and Skouboe 1975; Bollinger et al. 1985]. In principle, in order to perform Doppler cooling it suffices to apply a weak magnetic field to the ions and use a σ-polarised laser beam to push the population to the edges of the magnetic manifold in the $F = 2$ ground-state and the $F' = 3$ excited state and close the cooling cycle.

However, imperfection in the beam polarisation, like residual π-polarised light and the involved energy level structure in the $^2P_{3/2}$ state, can cause decays into the $F = 1$ ground state, which is a dark state in this configuration. To close the cooling cycle, an electro-optical modulator (EOM) modulates sidebands onto the cooling laser at a frequency of $1.25\,\mathrm{GHz}$ repumping the population from the $F = 1$ manifold.

3 Trap and Experimental Setup

In the first part of this chapter the design of the trap, its specific features and then how it is controlled and integrated into the setup is described. This is followed by a description of two laser systems involving optical resonators that were set up during the work presented here. Both are employed to generate light in the ultra-violet (UV) range of the electromagnetic spectrum in order to photoionize Beryllium atoms and laser cool the resulting ions, respectively.

3.1 Experimental Setup

Trap Design

The trap consists of two chips, fabricated by the group of Ron Folman at Ben Gurion-University in Israel, with a gold electrode structure lithographically applied onto them and a transparent, but electrically conducting, center electrode consisting of indium tin oxide (ITO), see Fig. 6. This allows fluorescence imaging of the $^9\mathrm{Be}^+$ ions through the chip, while preventing stray charges to accumulate due to the finite surface-resistance of the grounded ITO of $R_\square = 20(5)\,\Omega$. However, the additional grounded ITO electrodes between the RF rails modify the shape of the electric potential, which is quantified with electrostatic simulations, discussed in Ch. 4.1. The 2 µm thick gold electrodes are on top of a quartz glass substrate with a thickness of 2 mm. The RF rails are separated by the grounded ITO electrode in the center and surrounded by 22 pairs of DC electrodes. The DC electrodes have a width of 2 mm and are separated by a 75 µm gap from each other and by a 90 µm gap from the RF electrodes. The RF rails and the ITO center rail are 1 mm wide with 90 µm gap in between. At the relevant wavelength of 313 nm for Doppler cooling of $^9\mathrm{Be}^+$ ions, the total transmission through the ITO and the substrate was measured to be 30 %.

Having a mm-scale segmentation allows to shape the axial potential in order to move ions in the trap [Ruster et al. 2014; Kaushal et al. 2019], implement more involved capture and cooling procedures, as schematically shown in Fig. 7, and a precise transport to, for example, the precision trap of GBAR by extracting them from the trap [Jacob et al. 2016; Groot-Berning et al. 2019]. Since the goal is to trap a large beryllium-crystal one needs to cover as much trap volume with the cooling beam as possible, which requires the beam to be aligned with the trap axis. Additionally, the outer ions of a large cloud would experience large micromotion due to their distance from the RF-node, which would significantly broaden the line shape of the cooling transition and result in a higher Doppler cooling limit accoring to Eq.(39). To be able to decouple the laser beam from the

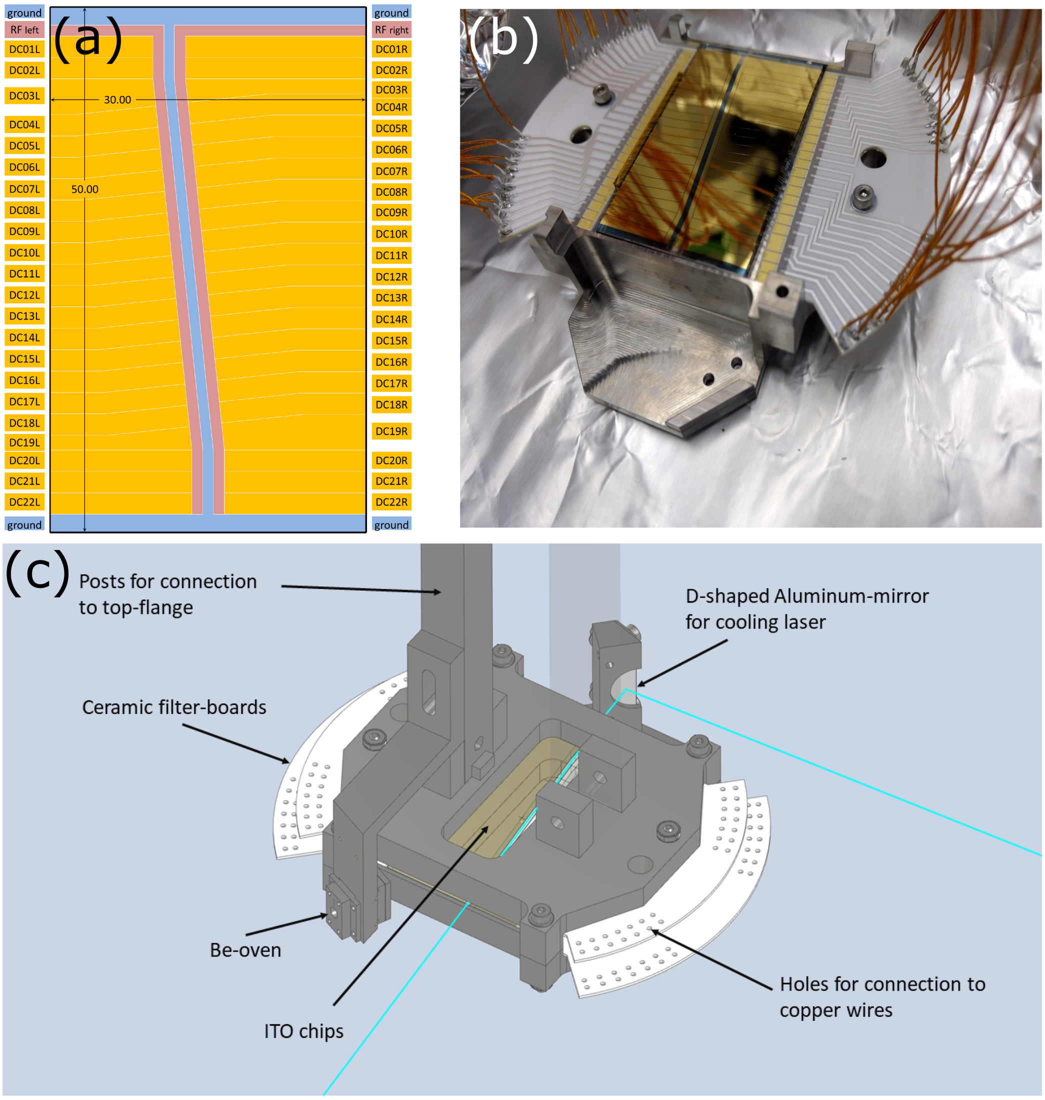

Figure 6: (a) design drawing of the lower chip with DC-electrodes in yellow, the RF-electrodes in red and ITO in blue; (b) Photograph of the lower chip in the support structure during assembly, already wire-bonded to the ceramic filter-board, with the copper wires soldered to it; (c) CAD-model of the stainless steel support structure, the trap chips UV-glued to them.

trajectory of the outgoing ions, an additional feature of the trap structure is the 6°-angle of the central RF rails after the first two pairs of DC-electrodes. This creates a RF guide to deflect the incoming ions. The trap itself consists of two mirror-imaged wafers facing each other.

Support Structure and Electrical Connections

The chips are glued to a stainless steel holding structure with an UV-curable adhesive, seen in the bottom of Fig. 6. Electrical connection to the electrodes is established with a gold wire-bond to a gold pad on a ceramic filter-board, which in turn provides connection to soldered copper wires, see the photograph in Fig.6.

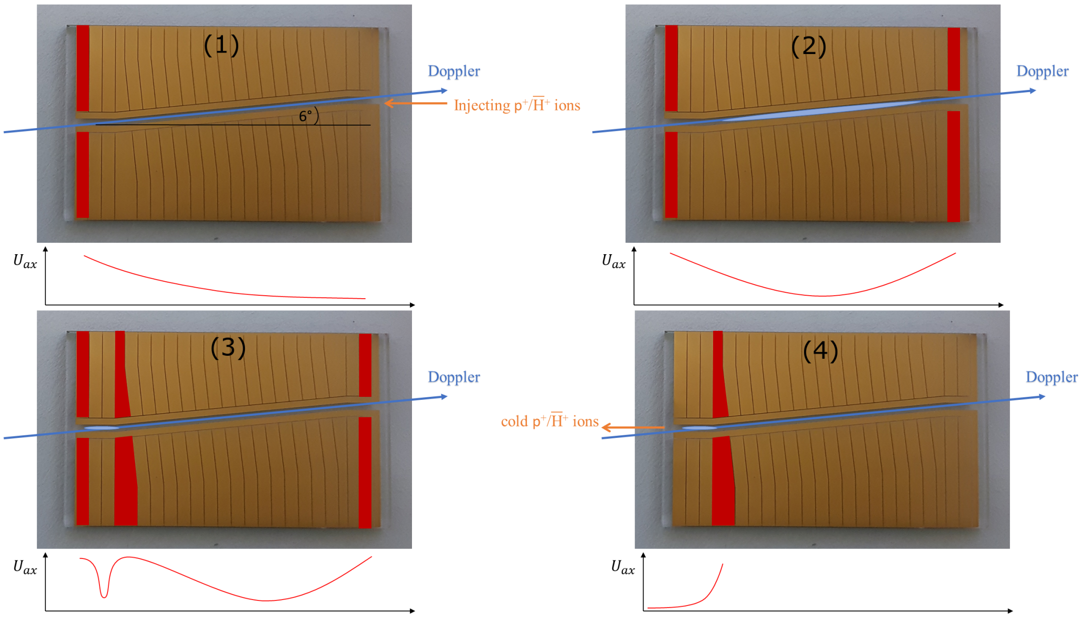

Figure 7: Envisioned, simplified sequence for the sympathetic cooling of $p^+/\bar{H}^+$: (1): the hot ions are slowed down in the trap; (2) the trap is closed and loaded with $^9Be^+$ coolant ions; (3) and (4) after thermalisation in the $^9Be^+$-crystal, the $p^+/\bar{H}^+$ are moved to the end of the trap and extracted.

To reduce RF-pickup by the DC-electrodes, 10 nF capacitors are connected to ground on the filter-boards as electrical low-pass filters. The ITO was grounded with conductive glue between the chip and the grounded holding structure. All 88 wires connected to the DC electrodes are grouped together in four 25-pin Sub-D connectors with a feed-through through the top flange, shown in Fig. 8. All individual connections of the electrodes to the pins of the Sub-D-25 connectors are displayed in Appendix A. The RF-electrodes are grouped into two pairs (top-left with bottom-right and vice versa) and connected with copper wires, which have the same length to keep dephasing of the signal at a minimum and are spatially separated from the DC-wires to reduce electrical pick-up. The trap is impedance-matched to 50 Ω with a helical resonator, described in more detail in [Jacob 2016], and driven with a 5 W- amplified[1] RF-signal at 17.6 MHz coming from a signal generator[2]. A 1:10 capacitive probe connected to an oscilloscope and in parallel to the trap RF electrodes allows to measure the voltage V_0. Using the 5 W amplifier a maximum voltage amplitude of 260 V is available.
The Beryllium oven consists of ceramic tube of about 1 cm length with four holes of a diameter of 500 µm. In one hole the Beryllium wire is inserted and kept in place by ceramic bond. A Tantalum wire is wound through the other three holes and heats the Beryllium. The Tantalum in turn is point-welded to a Molybdenum

[1] ZHL-5W-1, Mini-Circuits
[2] SMC 100A, Rhode & Schwarz

wire, which then connects to a Copper wire in a luster-terminal. An aperture reduces spattering and coating of the trap electrodes.

Vacuum Chamber and Imaging System

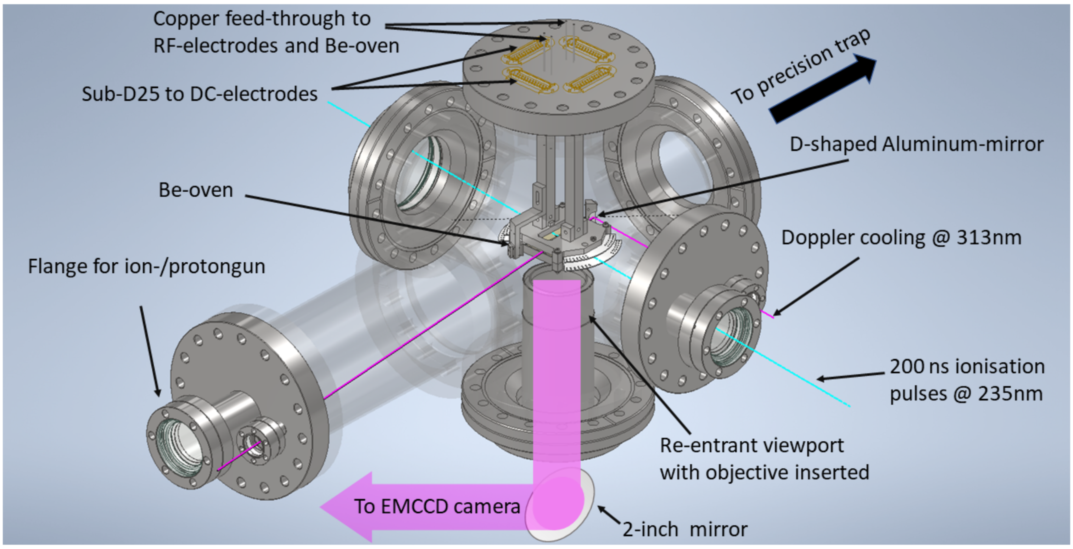

Figure 8: The vacuum chamber with the trap inserted from the top. More details can be found in the text.

The trap structure is inserted into the vacuum cross, shown in Fig. 8. The top-flange provides support of the trap and provides all electrical feed-troughs. On the bottom-flange an re-entrant viewport allows to insert an $f/1.6$ objective[3] to collect the fluorescence of the ions at a short distance and hence with a high numerical aperture. The objective design provides optimal imaging if the ions are at a distance of 40 mm away from the inner surface of the viewport, whose outer surface is supposed to be at a distance of 5.5 mm to the objective. The surfaces of the viewport and objective are anti-reflective coated for light at 313 nm ($R < 0.25\,\%$). The objective rests on a three-dimensional translation stage to focus the trap center onto the imaging system and a 5-inch mirror directs the light onto an EMCCD camera[4]. The Doppler cooling laser enters the chamber through an anti-reflection coated window, and leaves it again at the front side after reflection off the D-shaped mirror and propagation along the trap-axis. The photo-ionization beam is steered to the trap from the same side as the Doppler laser and then the chamber on the opposite side. The entire chamber is supported by steel posts mounted to an optical table.

[3]S6ASS2248/389, Sill Optics GmbH Co. KG
[4]ANDOR, iXon 860

3.2 Optical Systems for Ionization and Cooling

Resonant Photo-Ionization Laser

In order to efficiently load Beryllium ions in the trap, a two-photon, one-photon resonant process is used. The Beryllium atom is first resonantly exited from the $2s^2\,{}^1\mathrm{S}_0$ ground state to the $2s2p\,{}^1\mathrm{P}_1$ state at a wavelength of 234.9329 nm and then off-resonantly absorbs another photon that lifts it well above the ionization energy of 9.322 70 eV [Sansonetti and Martin 2005].
For this purpose, a pulsed Titanium:Sapphire (Ti:Sa) laser was utilized, that was already developed for loading ions in the precision trap and is described and compared to a non-resonant scheme with a frequency-quadrupled pulsed Nd:YAG laser at 266 nm in [Wolf et al. 2018]. It is adapted from a laser system used at RILIS/ISOLDE, where ionization experiments on radioactive beams are performed [Yi et al. 2003; Rothe et al. 2011]. The Ti:Sa crystal is pumped by a commercial frequency-doubled Nd:YAG pulsed laser[5] with a pulse length of roughly 300 ns at a repetition rate of 7 kHz and an avergage power of 12 W. The pump laser is focused to a waist of $w_0 \approx 100\,\mu\mathrm{m}$ with a $f = 90\,\mathrm{mm}$ lens and to improve its overlap with the fundamental mode of a Z-shaped, symmetric standing-wave cavity through one of the concave mirrors with radius $r = 75\,\mathrm{mm}$ forming the central arm of the resonator, see Fig. 9. The Brewster-cut Ti:SA crystal is placed in between the two concave mirrors at a distance of 20 mm to one and 50 mm to the other. The crystal has a length of 20 mm and a diameter 6 mm and is mounted in a water-cooled Copper block. Two highly reflective mirrors at the end of the outer arms confine the cavity to an optical length of 495 mm, resulting in a free spectral range (FSR) of 300 MHz, and leave enough space for wavelength selective elements. Coarse tuning of the fundamental wavelength to 939.73 nm is achieved with a birefrigent filter[6] and fine tuning with an etalon[7] ($d = 0.3\,\mathrm{mm}$, $R = 40\,\%$, FSR = 325 GHz). There is no active stabilization implemented in this version of the cavity to keep the wavelength constant, so that after turning on the pump laser, the cavity first has to reach an equilibrium, typically within half an hour and then drifts around the desired wavelength. A small fraction of the fundamental beam leaves the cavity through one of the end mirrors and is coupled into a fiber connected to a wavemeter for monitoring of the wavelength. The linewidth of the fundamental beam is 5 - 8 GHz while the pulses are 60 ns long. An intracavity barium borate (BBO) crystal, cut at an angle of 25.2° to fulfill phase matching, frequency-doubles the infrared beam into the the blue part of the spectrum, which is coupled out of the cavity with a dichroic

[5]ORC-1000, Clark-MRX Inc.
[6]Matisse Bifi 325, Sirah Lasertechnik
[7]Laseroptik GmbH

mirror. Finally, a last single-pass doubling step in a 58.2° cut BBO results in about 10 mJ of UV laser light at 235 nm.

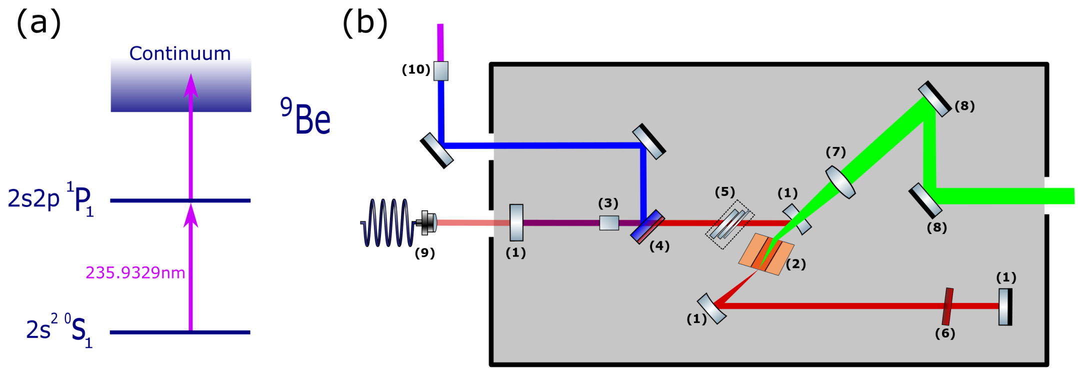

Figure 9: (a) Electronic level diagram of neutral Beryllium; (b) Schematic view of Ti:Sa cavity: (1) Resonator mirrors, (2) Brewster-cut Ti:Sa crystal in copper holder, (3) intra-cavity BBO, (4) dichroic mirror, (5) three-plate birifrigent filter, (6) etalon, (7) incoupling lens, (8) incoupling mirrors, (9) fiber coupler and fiber to wavemeter, (10) BBO for blue-to-UV frequency-doubling; further information can be found in the text.

Doppler Cooling Laser

Doppler cooling of ^{9}Be$^+$ ions is performed on the $S_{1/2} \rightarrow P_{3/2}$ transition at a wavelength close to 313 nm. Generating light at that wavelength is not straight forward and to our knowledge commercially available sources are extremely expensive. Different schemes of producing light at 313 nm were developed over time. They all have in common that they frequency-double a 626 nm laser in a second-harmonic generation (SHG) cavity, while differing in the way of how to generate that light at 626 nm.

A low cost but low power approach is based on commercially available diodes in a master-slave configuration used, for example, in the precision trap experiment [Cozijn et al. 2013]. At room temperature these diodes emit light at about 635 nm and hence have to be cooled to about −30 °C in order to shift the emission wavelength to 626 nm. For this work an alternative high power but high cost approach first developed at NIST [Wilson et al. 2011] based on sum-frequency generation (SHG) of two infrared (IR) fiber lasers, that were provided to us by the group of Laurent Hilico at Laboratoire Kastler Brossel in Paris, is used and explained in the following.

Fiber Laser Setup

In a first step, the two IR fiber lasers[8] at wavelenths of 1050 nm and 1550 nm are amplified by the suitable fiber amplifiers[9] from 10.6 mW and 23.8 mW to 540 mW and 460 mW, respectively, and brought via fibers to the optical breadboard shown in Fig.10. The two laser beams are then overlapped on a dichroic mirror and coupled into a fiber that guides the light to a Periodically-Poled Lithium-Niobate (PPLN) crystal[10]. Because of the symmetric collimators/fiber configuration, no additional beam shaping optics are required for the 1050 nm beam, and a telescope system with $f = 75$ mm for both lenses bridges the slightly larger distance between the collimators for the 1550 nm beam.
The total IR power entering the PPLN is about 1 W to not exceed the limit specified by the manufacturer. The dimensions of the crystal are 40 mm × 10 mm × 0.5 mm ($l \times w \times h$) and the relevant surfaces are anti-reflection coated for all of the three wavelengths involved to less than 1 % reflectivity. In order to maximize the quasi-phase-matching the crystal is heated up to about 175 °C and stabilised by an analog temperature servo at the temperature optimizing the generation of 626 nm light. A dichroic filter removes any residual IR light and then a polarisation-maintaining fiber guides the 626 nm laser to the SHG cavity. For wavelength monitoring, a 1:99 beamsplitter separates a small fraction of the beam, which is coupled into a fiber and sent to a wavemeter. The wavelength can conveniently be tuned by the fiber lasers, which have an integrated system to control the length of the lasing fibers by changing their temperature (maximum tuning range of roughly 1 nm for each of the IR lasers). At the maximum total IR input power of 1 W, we obtain 210 mW before entering the fiber, and 155 mW it.

SHG Cavity

The frequency-doubling of the 626 nm light takes place in a Beta-Barium-Borate (BBO) crystal. Because the conversion efficiency for single pass of a continuous wave through a nonlinear crystal is typically very low, an enhancement cavity is build around it [Franken et al. 1961; Armstrong et al. 1962; Ashkin, G. Boyd, and Dziedzic 1966]. The design of the cavity is adopted from [Koelemeij, Hogervorst, and Vassen 2005; Wilson et al. 2011; Cozijn et al. 2013; Hannig et al. 2018] and has a bow-tie shape as can be seen in Fig. 11.
A coherent build-up of SHG light with wavevector $\vec{k}_{\mathrm{SHG}}$ is only possible when the phase-matching condition with the wavevector of the pump light (PL) $\vec{k}_{\mathrm{PL}}$ is

[8]Koheras ADJUSTIK, NKT Photonics
[9]Koheras BOOSTIK, NKT Photonics
[10]MSFG626, Covesion Ltd.

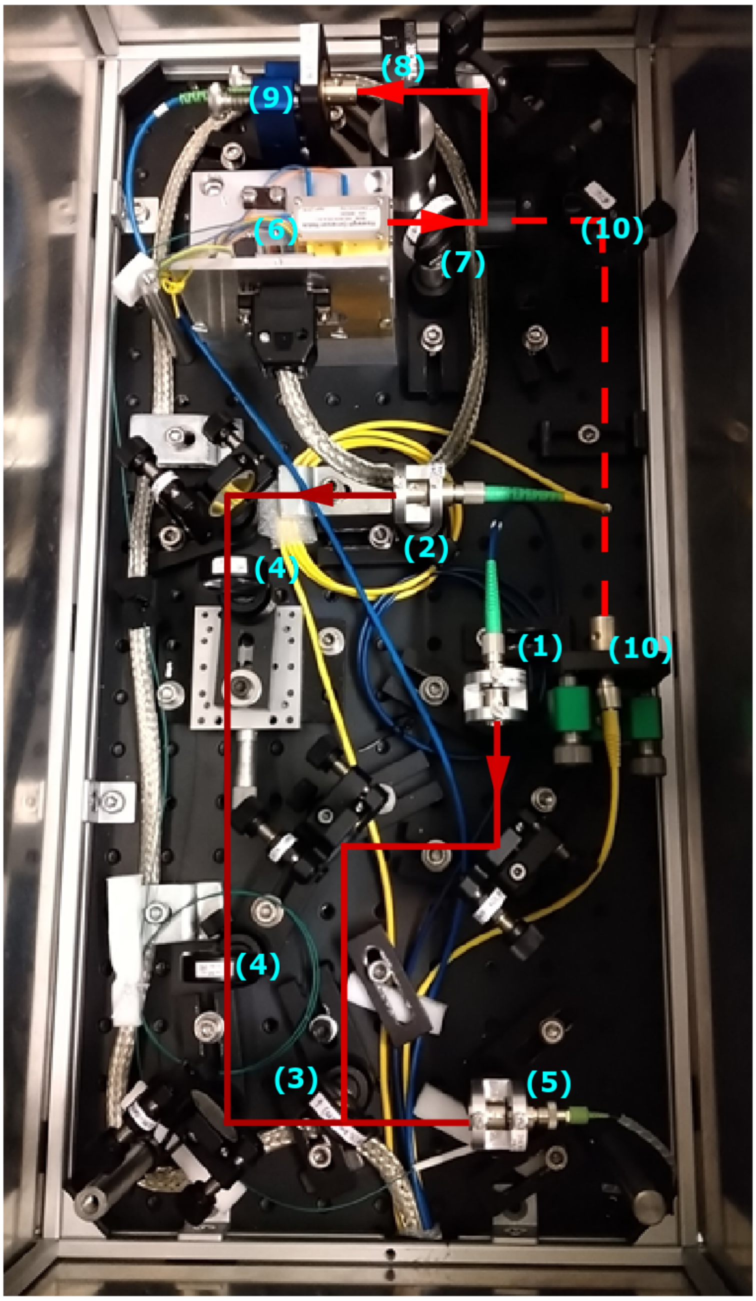

Figure 10: Photograph of the SFG setup; (1) output coupler of the 1050 nm laser, (2) output coupler of the 1550 nm laser, (3) dichroic mirror, (4) telescope system, (5) input coupler for the overlapped IR beams to PPLN fiber, (6) output coupler at the PPLN crystal ontop of oven, (7) dichroic filter and beamsplitter, (8) $\lambda/2$-waveplate at 626 nm, (9) fiber coupler to SHG cavity, (10) mirror and fiber coupler for wavelength monitoring.

fullfilled:

$$\vec{k}_{\mathrm{PL}} = 2\vec{k}_{\mathrm{SHG}}. \tag{40}$$

Since BBO exhibits chromatic dispersion, the refractive indices for the two wavelength are in general different resulting in destructive interference of SHG photons originating from different positions inside the crystal. However, one can exploit the birefringence of the crystal resulting in different refractive indices for light with polarisation perpendicular (called ordinary) to the optical axis of the medium, and light with polarisation parallel (called extraordinary) to it. Then, at a specific angle θ_{pm} between the wavevector and the the optical axis the phase-matching condition can be satisfied. In the case of SHG of 626 nm the specific phase-matching angle is

$$\theta_{\mathrm{pm}} = 38.4°. \tag{41}$$

There are two main steps of optimization that led to the present design of the cavity, namely, in a first step, the power generated per single pass is maximized for given crystal dimensions and properties, and in a second step, a cavity configuration is obtained to meet those requirements and maximize the power enhancement.

In the limit of low conversion efficiency and hence nearly undepleted pump light (in this case $< 500\,\mathrm{mW}$ [Wilson et al. 2011]), the power of the SHG light P_{SHG} scales with the square of the pump light power P_{PL}

$$P_{\mathrm{SHG}} = \kappa P_{\mathrm{PL}}^2, \tag{42}$$

with κ being the conversion coefficient. For a crystal of about a centimeter length κ is on the order of $10^{-4}\,\mathrm{W}^{-1}$. The reason for this is that the power generated per infinitesimal crystal volume is proportional to the pump light intensity squared. This poses the optimization problem of finding the best ratio of given crystal length l to focus of the Gaussian beam with waist w_0 , since a tighter focus inside the crystal yields higher intensity but in turn increases the divergence of the beam and reduces the intensity away from the focus. This was investigated in [G. D. Boyd and Kleinman 1968] and the optimum focusing ratio l/b of 2.84 was found, with $b = w_0^2 k$ being the confocal parameter, when considering a circular Gaussian beam and neglecting birefringence. One consequence of taking birefringence into account is that the Poynting vectors of the PL beam and the SHG are in general not parallel which results in a so-called walk-off angle ρ and in the case here $\rho = 4.6°$ [Hannig et al. 2018]. Hence, in order to maintain a sufficient overlap of the two beams a weaker focusing of the pump light is necessary. In this case

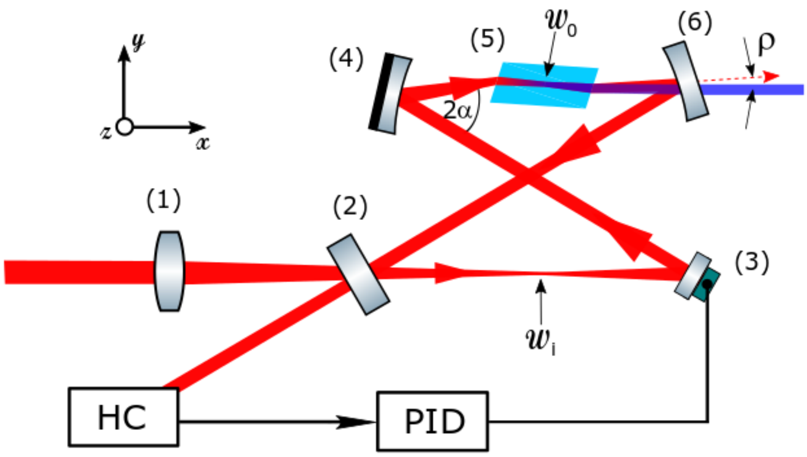

Figure 11: Schematic of the SHG cavity with (1) incouping lens, (2) incoupling mirror, (3) piezo actuator, (4) and (6) spherical mirrors with r = 30 mm, (5) Brewster-cut BBO.

the Boyd-Kleinman model yields the ratio $l/b = 1.42$ and thus for a 12 mm long BBO and the SHG considered here results in $w_0 = 20.5\,\mu\text{m}$.

To keep reflections from the surfaces of the crystal minimal the BBO is Brewster-cut, where the Brewster angle is given by

$$\theta_\mathrm{B} = \arctan \frac{n_1}{n_0}, \tag{43}$$

and for the transition from air to BBO with refractive indices $n_0 = 1.00$ and $n_1 = 1.66$, respectively, equals 59.0°. But inserting a Brewster-cut element to the systems causes astigmatism, resulting in different waists in the sagittal plane (the plane in which the beam propagates, xy-plane in Fig. 11), and the tangential plane (the plane perpendicular to the sigittal plane, xz-plane in the figure). One way to compensate for this is by directing the beam onto spherical mirrors[11] with an angle α to normal incidence. In turn it is now necessary to use another two (planar) mirrors to be able to close the cavity and the bow-tie configuration suggests itself, having the additional feature of preventing standing-wave formation. The radius of curvature and the distance to the crystal of the mirrors also define the waists inside the BBO. A stable configuration for both, the sagittal and tangential component, can be found and brought close to the optimum [Wilson et al. 2011; Freegarde et al. 1997] by using the parameters summarized in Tbl. 1, which are taken from [Heinrich 2018], where the same cavity version is used.

The cavity is most efficiently excited when the beam matches the mode of the

[11] Laseroptik GmbH

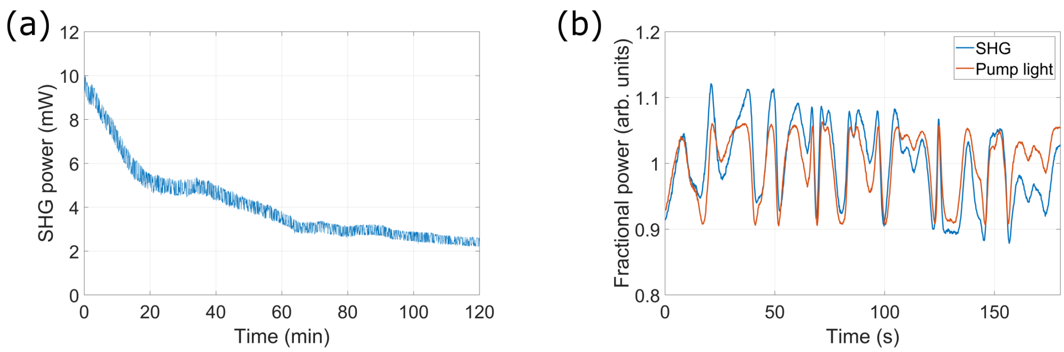

Figure 12: (a)SHG power at 313 nm recorded over two hours; (b) Fractional SHG power (blue) together with fractional PL power (red) recorded over three minutes, the the SHG power-fluctuations are caused by fluctuation of the pump light power.

cavity and for this purpose a lens with $f = 100$ focuses to the right incoupling waist $w_i \approx 90\,\mu\text{m}$. Besides mode-matching, also impedance matching has to be taken care of, meaning that the transmission T of the incoupling mirror has to be chosen in such a way that is compensates for all the losses inside the cavity. Since this is difficult to estimate under real conditions, different transmission coefficients $T = 0.7\,\%$ $T = 1.2\,\%$ and $T = 1.8\,\%$ were tested, where the latest gave the best results. Finally, the cavity is stabilised by a Hänsch-Couilllaud [Hansch and Couillaud 1980] locking scheme with feedback to a small second planar mirror mounted on a piezo actuator.

Overall we obtain an output power $P_{\text{SHG}} \approx 10\,\text{mW}$ when pumping with $P_{\text{PL}} = 155\,\text{mW}$, which is well in agreement with [Wilson et al. 2011; Heinrich 2018]. However, the SHG power decreases over time as shown in Fig. 12(a) to a significant fraction of the maximum output power and usually settles at 3 mW to 5 mW. After carefully cleaning the mirrors inside the cavity one is back at the maximum output power, hence we assume that the long-term (hour-scale) degradation is caused by dust particles accumulating on the mirrors. The short-term (second-scale) fluctuations shown in Fig.12(b) can be attributed to instabilities in the SFG of the 626 nm light, since the two IR fiber lasers do not show these fluctuations.

Electro-Optic Modulator

EOM's rely on the electro-optic effect of nonlinear crystals, by which the refractive index of the crystal can be changed by applying an electric field to it. For a linearly polarized beam entering the crystal this would in principle result in an elliptical polarization after propagation through the medium. This can be avoided

BBO dimensions	$l \times w \times h = 12 \times 4 \times 4$
phase-matching angle	$\theta_{\mathrm{pm}} = 38.4°$
Brewster's angle	$\theta_{\mathrm{B}} = 59.0°$
radius of curvature of mirrors	$r = 30\,\mathrm{mm}$
incident angle on curved mirrors	$\alpha = 19.5°$
distance crystal and curved mirrors	14.6 mm
geometric roundtrip length	185 mm
sagittal waist in crystal	$w_0^{sag} = 21.3\,\mu\mathrm{m}$
tangential waist in crystal	$w_0^{tan} = 30.9\,\mu\mathrm{m}$
incoupling sagittal waist	$w_i^{sag} = 88.7\,\mu\mathrm{m}$
incoupling tangential waist	$w_i^{tan} = 92.4\,\mu\mathrm{m}$
geometric roundtrip length	$l_{rt} = 184.9\,\mathrm{mm}$

Table 1: SHG cavity parameters, partly taken from [Heinrich 2018].

by aligning the polarization with the optical axis of the crystal, so that an electric field will only cause a phase shift of the light wave. If one now applies a time varying electric field at a specific frequency, the phase of the laser beam will be modulated and sidebands at that frequency will appear. In the first stage of the experiment an EOM[12], where the nonlinear crystal consisted of potassium-phosphate (KDP), which was integrated into a resonant high-Q RF circuit tuned to the relevant frequency of 1.25 GHz. With this model one has to apply an RF power of 33 dBm to achieve a modulation depth of 1 rad. Such high powers usually result in heating of the system, which has a drift of the resonance frequency of the RF circuit as a consequence, so that an active temperature control has to be integrated for a stable operation. During this work, the supplier provided a new version of the EOM relying on crystal (whose composition was not exactly specified) exhibiting a larger electro-optic effect, so that for a modulation depth of 1 rad only 14 dBm of RF power are required, what promises a more stable operation. While KDP has a transmission of $T = 95\,\%$ for light at a wavelength of 313 nm, the drawback of the new crystal material is a larger absorption coefficient. Especially, it is not well known at which intensities nonlinear absorption effects start to matter and could potentially damage the crystal. For that purpose the 313 nm beam was focused to an elliptical waist of $55\,\mu\mathrm{m} \times 90\,\mu\mathrm{m}$ with a $f = 200$ lens inside the crystal and transmission was measured for different input power, shown in Fig. 13. Up to a maximum intensity of $0.32\,\mathrm{W/mm^2}$ a transmission of $T = 62\,\%$ is observed with no rapid drop indicating nonlinear absorption effects.

[12] QUBIG, PM-Be$^+$-1.3

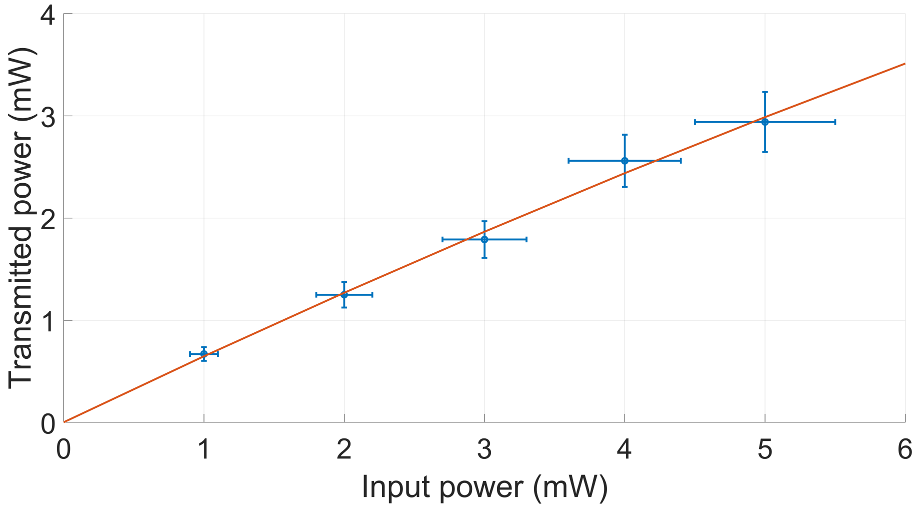

Figure 13: Measured output power of the Doppler cooling beam for different input powers in blue. The error bars correspond to 10 % of the measured value as these are the short term power fluctuations, see Fig.12(b). A second-order polynomial fit (orange) shows that in this intensity regime the ouput power is linearly dependent on the input power with a negligible quadratic term.

4 Trap Simulations and First Observed Beryllium Ions

4.1 Simulations

Radial Electric Potential

In order to characterize the trapping of ions for different experimental parameters the electric potential of the trap is calculated using COMSOL Multiphysics software. In Fig. 14 two-dimensional electrostatic simulations of the cross-section of the electric potential and the electric field norm squared, which is proportional to the pseudopotential [Eq. (18)], are compared. All the electrodes, including the ITO, are modelled as ideal conductors and a negligible dependence of the electric potential along the symmetry axis (z-axis by adopting the convention from Ch. 2.1) is assumed. Fig. 14(a) shows the electric potential, when a test voltage of 2 V is applied to one pair of RF electrodes, while the others are held at ground, the corresponding square of the electric field norm is shown Fig. 14(b). Fig. 14(c) and (d) show the situation, where both electrode pairs are driven with one RF signal being phase-shifted by π, which is modelled by holding one pair at a +1 V and the other at -1 V, keeping the overall potential difference of 2 V. In both cases the electric potential was fitted by a parabolic function

$$\Phi(u) = \frac{\Phi_0}{2r_0^2}u^2 + \Phi_{\text{offset}} \tag{44}$$

along both axes $u = x, y$. As an example, in Fig. 14(g) the simulation data and the corresponding fit in dashed lines are shown for the out-of-phase driving. Only the points around the origin, indicated by the dashed vertical line in black are included in the fit. All fits reveal an effective trap radius of $\tilde{r}_0 = 1.54$ mm, close to the expected $r_0 = 1.41$ mm. Considering this we can estimate the relevant trap characteristics derived in Ch. 2.1 For example, driving at maximum $V_0 = 250$ V will result in an stability parameter [Eq.(7)] $q = 0.38$.

Estimating the radial trap depth by using the pseudopotential approximation is not that straight forward, since one has to consider in what volume the electric potential and hence the pseudopotential is mainly of quadrupolar shape. In order to visualize this the square of the electric field norm, which is proportional to the pseudopotential, is plotted on the right-hand side of Fig. 14. The white dashed lines in Fig. 14(b) and (d) indicate the axis of the smallest electric field, as a measure of the lowest confining pseudopotential. The square of the electric field norm along these axis is plotted in Fig. 14(h) in red and blue. The dashed lines in the same colours result from a parabolic fit along the direction of lowest confinement. Also here only points around the origin, indicated by the dashed horizontal line in black, are included. The solid horizontal line indicates the position where the deviation of the fit from the data is less than 1 % so that the ion's motion, in good approximation, is actually described by the Mathieu equations [Eq.(8)]. In both cases one can infer that the simulated pseudopotential should agree with that of an ideal Paul trap within a radius of about 200 µm. Using this, the pseudopotential can be calculated at that distance from the center, which amounts to 100 meV, again at the maximum driving voltage of $V_0 = 250\,\mathrm{V}$. The prefactor

$$\kappa = \frac{Q^2 V_0^2}{4m\Omega_{RF}^2 r_0^4} \tag{45}$$

in Eq.(18) corresponds to the curvature of the pseudopotential and amounts to $2.7\,\mathrm{eV/mm^2}$. This will become important when we compare it to anti-confinement of the applied axial voltage later in this section.

We also can conclude, as expected, that driving one or two pairs of RF electrodes does not change the overall trap depth when the same voltage difference is applied. In Fig. 14(d) it is clearly visible, that having the grounded ITO electrode in between the RF electrodes has an effect on the pseudopotential shape. In order to quantify this further, additionally the electric potential without the ITO was simulated and the results are shown in Fig. 14(e) and (f). The effective trap radius $\tilde{r}_0$ is the same as in the previous electrode configuration, but, as it can be seen by the green curve in Fig. 14(h), the achievable radial trap depth is at least a factor of two larger compared to the case with the ITO electrodes.

Furthermore, it is worth noting, that the choice of the coordinate system in the present trap geometry is ambiguous. While in a classic linear Paul trap the aligning the radial coordinate axes along the axis of the RF electrode pairs suggests itself and usually any asymmetry of the potential along the x- and y-directions created by the axial potential can be taken into account by modifying the geometric factors $\alpha \neq -\beta \neq 1/2$. In our case we will define a second set of radial axis to be parallel and perpendicular to the plane of the chips, x' and y' in Fig. 14(a) and (c), which will make it more convenient to discuss the effects of the axial potential in the next section.

Axial Electric Potential

In order to estimate the axial electrical potential the three-dimensional structure of the trap has to be taken into account. We simplified the geometry by only modelling five DC electrodes on each side. In Fig.15(a) the red electrodes are hold at test voltage of $U_{\mathrm{ax}} = +1\,\mathrm{V}$ with a gap of one grounded DC electrode in between. The curves in Fig.15(b) show the potential around the origin along the coordinate

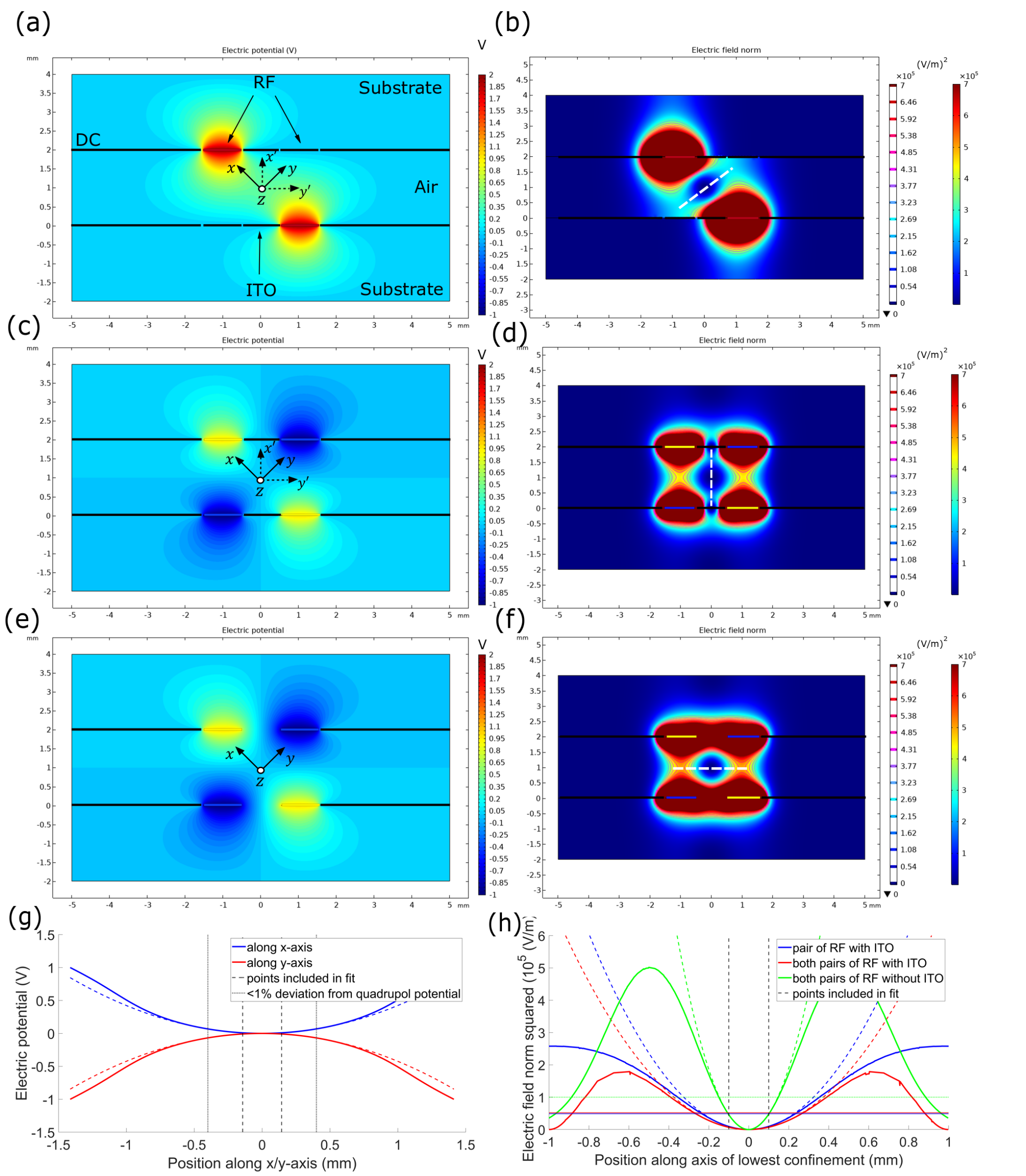

Figure 14: Two-dimensional electrostatic static simulations of the radial trap potential: (a) 2 V applied to one pair of RF electrodes with corresponding electric field norm in (b); out-of phase driving of with ITO electrode (c) and without (e) with the corresponding electric field norm in (d) and (f), respectively; (g) shows potential along the two radial directions for the simulation in (c); (h) comparison of the the electric field amplitude as a measure of the pseudopotential along the axis of lowest confinement for three cases above.

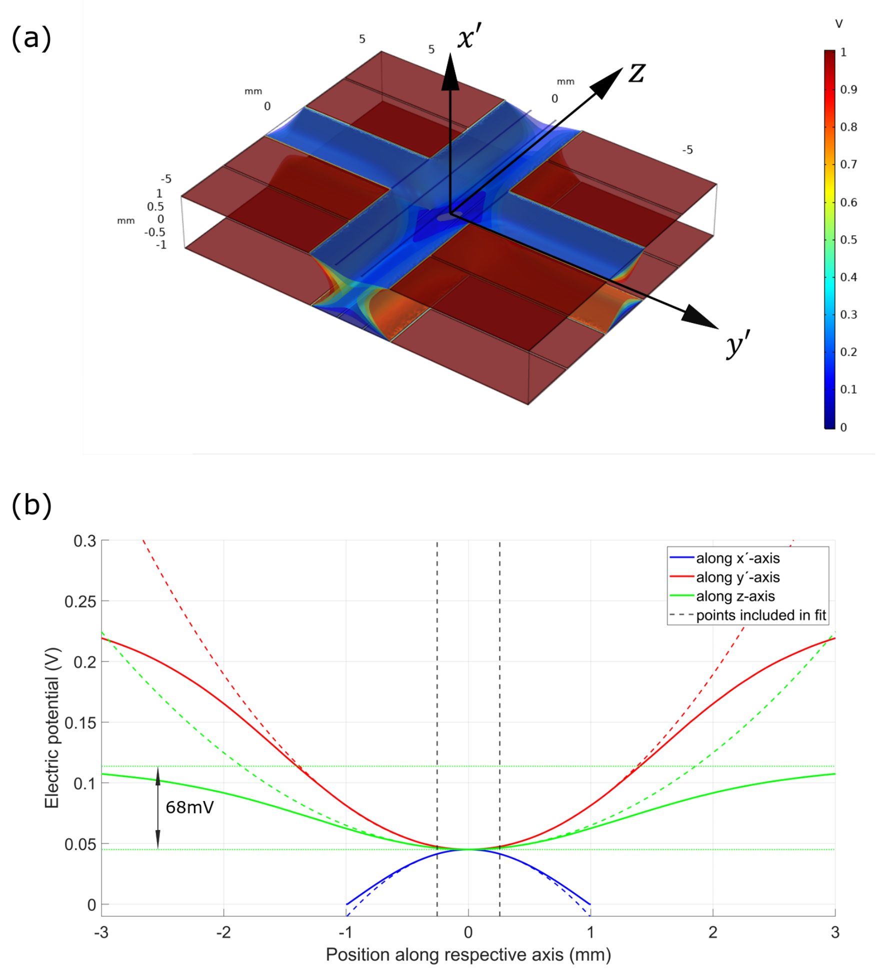

Figure 15: (a) Simulation of the axial trap potential modelled with five DC electrodes, where those in the center (blue) are held at ground potential and the outer ones (red) are held at 1 V; (b) electric potential along the axis indicated in (a) with parabolic fits to them within the dashed lines.

axis as chosen in the above figure, again the dashed lines show parabolic fits in the respective colours. First thing to notice is the low conversion of applied voltage to axial trap depth of 68 meV, compared to a conventional segmented linear trap, where 500 meV would be expected, like for the trap operated in [Heinrich 2018]. Secondly, regardless of the low axial confinement, the anti-confinement along the x'-axis is quite large. This is because of the aspect ratio of the trap, more precisely, the distance of the trap center to the grounded ITO is 1 mm while the minimal distance of two DC electrodes is 2 mm. This also justifies the choice of the coordinate system since we would like to have one of the axes along the direction of largest anti-confinement. To quantify this further, let us look at the results of the fits, where the potential around the origin is kept in its more general form:

$$\Phi(x', y', z) = \alpha x'^2 + \beta y'^2 + \gamma z^2 + \Phi_{\text{offset}}. \tag{46}$$

The strength of the anti-confinement is given by the curvature α in Eq.(46), which the fit reveals to be $-0.056\,\mathrm{eV/mm^2}$. We can compare this to the confinement [Eq.(45)] and calculate the relative strength of anti-confinement and confinement $|\alpha/\kappa| = 2\,\%$.

trap used in	U_{ax}	V_0	stability parameter q	axial trap depth	α/κ
this work	1 V	250 V	0.38	68 meV	0.02
this work	1 V	66 V	0.1	68 meV	0.28
this work	10 V	250 V	0.38	680 meV	0.20
this work	10 V	66 V	0.1	680 meV	2.95
[Heinrich 2018]	9 V	259 V	0.13	4.5 eV	0.09
[Ann et al. 2019]	265 V	418 V	0.15	$\approx$ 5.5 eV	0.02

Table 2: Characteristic trap parameters for different axial voltages U_0 and RF voltages V_0 based on the electrostatic simulations and compared to other traps, where large Coulomb crystals were formed.

In Tbl. 2 different voltage configurations and their consequences on the electric potential are compared. For instance, in the second row $V_0 = 66\,\mathrm{V}$ results in the desired stability parameter of $q = 0.1$, but has a low axial confinement and a rather large anti-confinement as a result. For this set of parameters, using Eq.(22) one can find the trap frequencies $\omega_{x'} = 1856\,\mathrm{kHz}$, $\omega_{y'} = 2105\,\mathrm{kHz}$ and $\omega_z = 462\,\mathrm{kHz}$. If one wants the axial confinement to be deep enough to cover the whole velocity distribution of the the Beryllium, one has to apply $U_{\mathrm{ax}} = 10\,\mathrm{V}$, like in the third and fourth row. The parameters in the third row convert to trap frequencies $\omega_{x'} = 7213\,\mathrm{kHz}$, $\omega_{y'} = 7866\,\mathrm{kHz}$ and $\omega_z = 1462\,\mathrm{kHz}$, while trapping with parameters in the fourth row is not possible, since in this case the anti-confinement is larger than the confinement. Additionally, these values are compared to two other traps, in which large crystals of $^9\mathrm{Be}^+$ were trapped in last two rows. Clearly, the applied voltages are not directly comparable, since the geometry of these traps deviate from ours, but the other values might be worth keeping in mind as a reference. Of course, this entire analysis reflects only the case where one DC electrode is grounded between two others with a voltage applied to them, as in Fig. 15. Since this might not be ideal to trap large ion crystals, different configurations, leaving more DC electrodes as a gap were tried.

4.2 First Observed Beryllium Ions

Field of View Calibration

The most convenient way to focus the imaging system on the trap center was to direct the Doppler laser onto one of the chips and to observe the resulting scattered light. This made it possible to identify the different surface components, as shown in Fig. 16 and the known gap width of 90 µm allows for a length calibration of the field of view (FoV). According to this calibration one pixel of the camera shows a 2.3 µm × 2.3 µm section and with the physical dimensions 24 µm × 24 µm of one pixel this results in a magnification of about 10 meaning that we see a 290 µm × 290 µm part of the trap. The 45°-angle of the image is a consequence of the trap axis being at that angle with respect to the optical axis of the camera. In the left-hand side of Fig. 16 the small solid box illustrates that we can only observe a very limit region of the trap at the same time and the dashed box shows the region that maximally accessible by adjusting the translation stage of the objective and the mirror that directs the light onto the camera. For searching ions this means that there is always uncertainty whether the region looked at is really the trap center and the FoV has to be moved along the axis in time consuming fashion.

First Observed Beryllium Ions

For the initial search the DC-electrodes were grouped in the configuration indicated by the red and green shading in Fig. 16. The DC-voltages, $U_{\mathrm{ax},0}$ for the

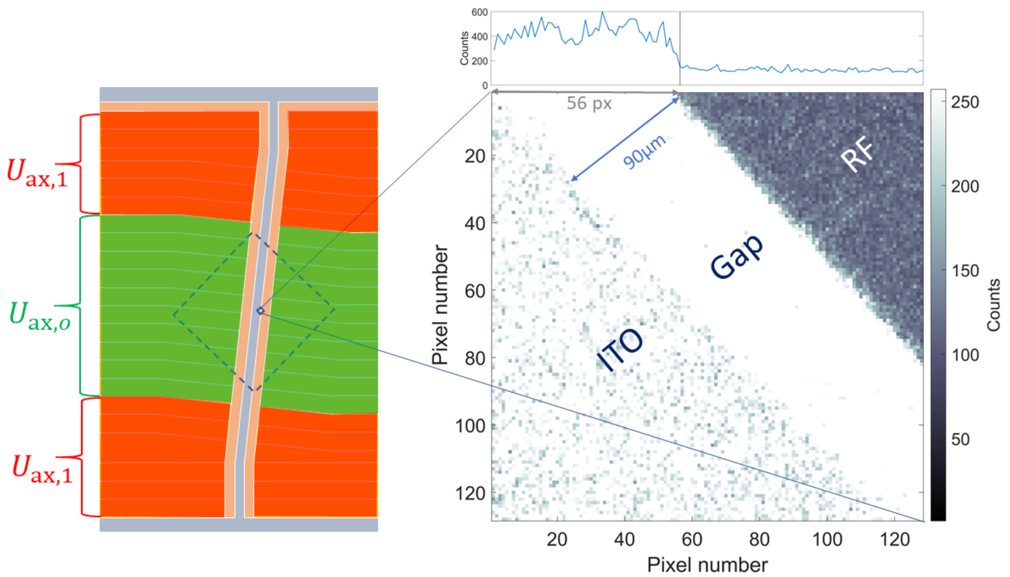

Figure 16: On the right-hand side the cooling laser is directed onto one of the trap chips, which allows to calibrate the field of view of the camera (illustrated by the solid box on the left side) as explained in the text. The dashed box on the left roughly indicates the maximally accessible region of the trap chips. The red and green shading of the electrodes on the left indicated which of them are grouped together and held at the same voltage for the initial trapping attempts (mirrored configuration on the top chip).

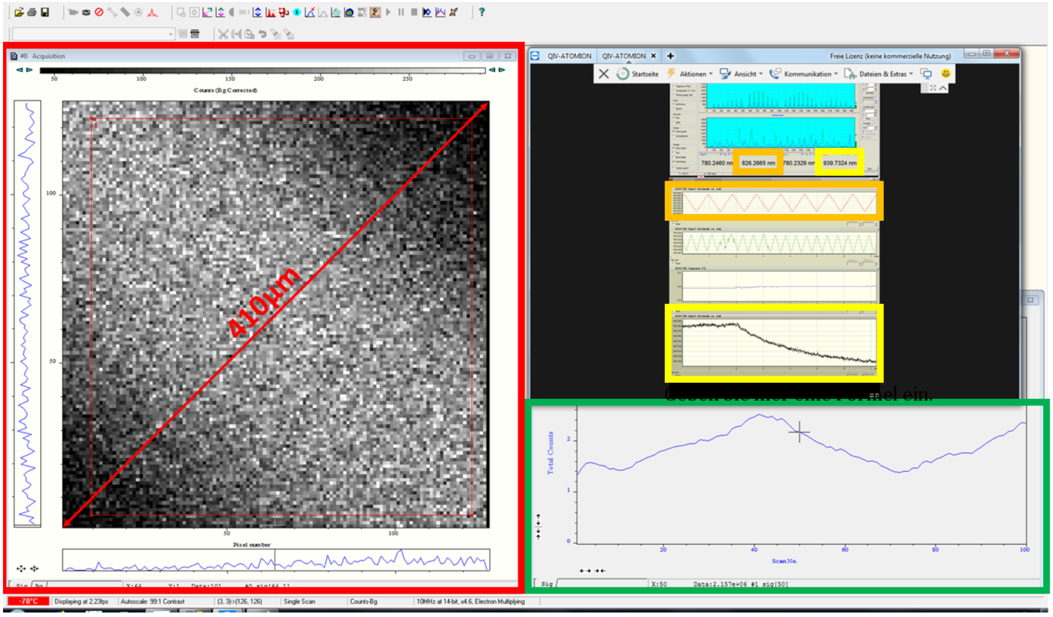

Figure 17: Screenshot of First Trapped Beryllium Ions: In the red box the camera image with part of a cloud of Beryllium ions along the trap axis is visible. The total photon count is shown in the green box. Its triangular modulation originated from the a wavelength modulation of the 626 nm laser of the same shape. The wavelength of the fundamental mode of the Ti:Sa cavity is highlighted b in yellow.

inner ten electrodes and $U_{\mathrm{ax},1}$ for the outer ones, are provided by an National Instruments card[13] with two analog outputs ranging from -10 V to +10 V. After increasing the current from its typical value of 3 A to more than 4 A fluorescence could be observed. The other essential parameters can be found in Tbl. 3. The oven construction could not sustain such high temperatures for more than about five hours. The ceramic tube containing the Beryllium wire is mainly supported and hold into place by the tantalum wire that also acts as the heat source, bent down and probably most of the Beryllium atoms were blocked by the oven aperture. Also a more stable wiring of the Beryllium oven could not sustain the temperatures necessary to observe ions in a subsequent run. Nonetheless, during the time with a signal we could confirm that we indeed observe Beryllium ions (turning the RF off and blocking the photoionization beam resulted in loss of the signal) and their behaviour on changing most of the experimental parameters were studied, even though profound experimental data could not be taken due to the short time. In the following the key observations from the time with ions are listed in order to draw conclusions for future searches at moderate oven currents:

- The radial extend of the ions cloud of 400 µm, see red box in Fig.17, being in good agreement with the simulation of the radial trap potential, which suggest that in this volume the ions equations of motions are well described

[13] USB-6002, National Instruments

by the Mathieu equations in Fig. 14.

- Turning off the RF-driving resulted in losing the signal, as expected, and going below an amplitude $V_0 = 230\,\mathrm{V}$ also had loss of the ions as a consequence.

- The total collected fluorescence (green box in Fig. 17) of the camera shows the same triangular modulation as the wavelength modulation of the pump laser about 626.2662 nm with a modulation depth of 350 MHz (orange boxes in Fig. 17). Most likely this originated from approaching the resonance of the ions.

- Raising the outer voltage $U_{\mathrm{ax},1}$ to the maximum of +10 V also resulted in a maximum of fluorescence, the ions were suddenly lost when the inner voltage $U_{\mathrm{ax},0}$ was set to less than -3 V.

- A peak in the brightness was observed when the fundamental mode of the Ti:Sa cavity reached 939.7311 nm, showing the expected resonant increase in photoionization when exciting the $2s^2\,{}^1\mathrm{S}_0 \leftrightarrow 2s2p\,{}^1\mathrm{P}_1$.

- When the photoionization beam is blocked, the ions where lost faster than the exposure time of the camera (shortest exposure time was 0.2 s).

- At an oven current of 3 A no fluorescence was observed even at the exposure times longer than 2 s

Camera exposure time	$0.8\,\mathrm{s}$
EM gain	150
Be-oven current	$> 4\,\mathrm{A}$
Cooling laser power	$P_{\mathrm{SHG}} \approx 3\,\mathrm{mW}$
Cooling laser beam diameter	$1\,\mathrm{mm}$
Cooling laser polarization	σ^+
EOM	not used at that point
Magnetic field current	$2.6\,\mathrm{A}$
Photoiionization laser power	$P_{235} \approx 10\,\mathrm{mW}$
Inner DC-voltage	$U_{\mathrm{ax},0} = -3\,\mathrm{V}$
Outer DC-voltage	$U_{\mathrm{ax},1} = +10\,\mathrm{V}$
RF-voltage	$V_0 = 260\,\mathrm{V}$
Pressure with Be-oven off (on)	$7.8 \times 10^{-10}\,\mathrm{mbar}(\approx 2.5 \times 10^{-8}\,\mathrm{mbar})$

Table 3: Experimental Parameters for First Trapping

5 Conclusion and Next Steps

The main obstacle at the moment is the short lifetime of ions in the trap. The time with ion signal was primarily used to adjust the trap parameters such that the oven temperature could be reduced while maintaining loaded ions, which was not achieved. Dark pumping of the ions is most likely ruled out by subsequent implementation of the EOM and establishing a closed cooling cycle. Correct operation of the EOM was confirmed by observing sidebands at 1.25 GHz with a cavity. Since the lasers seem not to be the problem, the working hypothesis is that either the trap parameters are chosen poorly or there is still a problem with the atomic oven. For now, different DC-electrode configurations are tried, for example, leaving a gap of only one grounded DC-electrode, while the other parameters are scanned. In a next step, a modified helical resonator will allow driving of both pairs of RF-electrodes. If these steps also fail, the vacuum chamber will have to be opened and in order to confirm that the oven does not have major damages and that all DC-electrodes are addressed correctly. Another path forward is a full dynamic simulation of trap, by modelling ion trajectories inside the trap and extracting the relevant parameters and further characterizing the effect of the ITO center electrode. For instance, previous SIMION-simulations performed in the group of Laurent Hilico showed that at kinetic energies of 100 meV the ions start leaking out of the trap towards the ITO electrode, supported by the simulations done in this work.

A Appendix

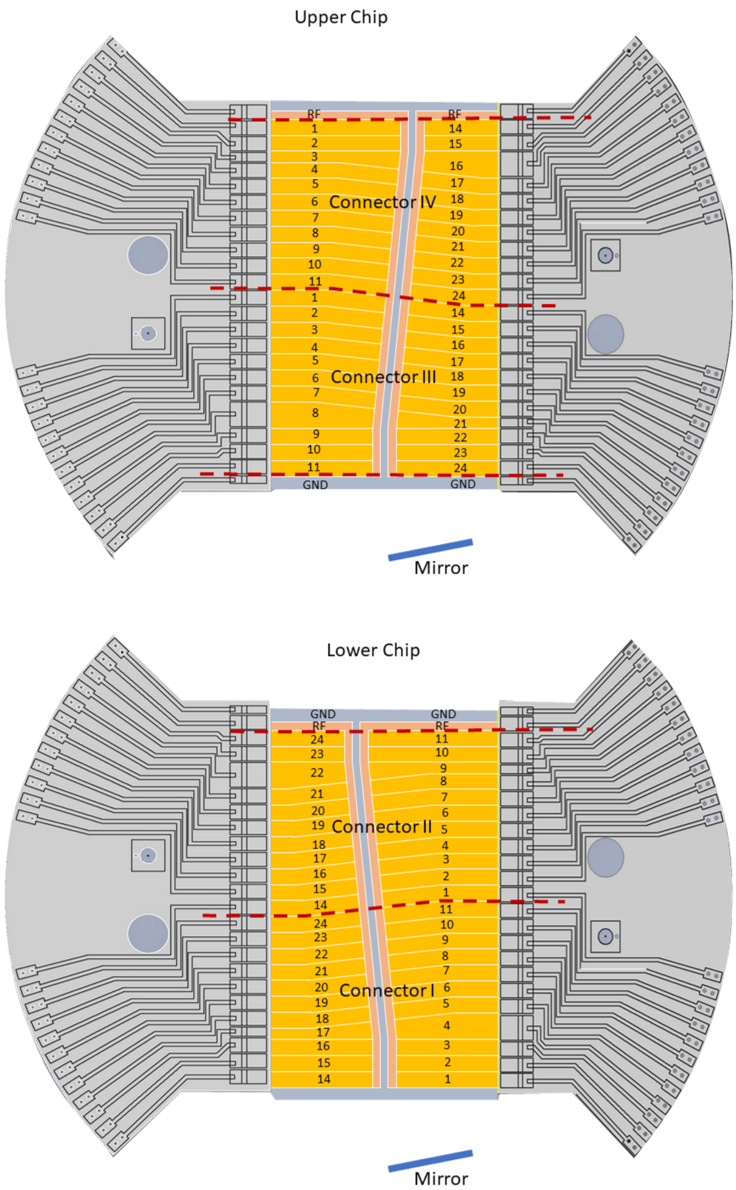

Figure 18: Layout of Pin-to-Electrode-Connections

References

Ahmadi, M., B. X. R. Alves, et al. (2020). "Investigation of the fine structure of antihydrogen". In: *Nature* 578.7795, pp. 375–380. ISSN: 1476-4687. DOI: 10.1038/s41586-020-2006-5. URL: https://doi.org/10.1038/s41586-020-2006-5.

Ahmadi, M. et al. (2018a). "Observation of the 1S–2P Lyman-α transition in antihydrogen". In: *Nature* 561.7722, pp. 211–215. ISSN: 14764687. DOI: 10.1038/s41586-018-0435-1.

— (2018b). "Observation of the 1S–2P Lyman-α transition in antihydrogen". In: *Nature* 561.7722, pp. 211–215. ISSN: 14764687. DOI: 10.1038/s41586-018-0435-1.

Amole, C. et al. (2013). "Description and first application of a new technique to measure the gravitational mass of antihydrogen". In: *Nature Communications* 4, pp. 1–9. ISSN: 20411723. DOI: 10.1038/ncomms2787.

Anderson, C. D. (1933). "The positive electron". In: *Physical Review* 43.6, pp. 491–494. ISSN: 0031899X. DOI: 10.1103/PhysRev.43.491.

Ann, B.-m., F. Schmid, J. Krause, T. W. Hänsch, T. Udem, and A. Ozawa (2019). "Motional resonances of three-dimensional dual-species Coulomb crystals". In:

Armstrong, J. A., N. Bloembergen, J. Ducuing, and P. S. Pershan (1962). "Interactions between light waves in a nonlinear dielectric". In: *Physical Review* 127.6, pp. 1918–1939. ISSN: 0031899X. DOI: 10.1103/PhysRev.127.1918.

Ashkin, A., G. Boyd, and J. Dziedzic (1966). "Resonant Optical Second Harmonic Generation and Mixing". In: *IEEE Journal of Quantum Electronics* 2, pp. 109–124. DOI: 10.1109/JQE.1966.1074007.

ATLAS-Collaboration, T. et al. (2012). "Observation of a new particle in the search for the Standard Model Higgs boson with the ATLAS detector at the LHC". In: *Physics Letters, Section B: Nuclear, Elementary Particle and High-Energy Physics* 716.1, pp. 1–29. ISSN: 03702693. DOI: 10.1016/j.physletb.2012.08.020. arXiv: 1207.7214.

Bollinger, J. J., J. S. Wells, D. J. Wineland, and W. M. Itano (1985). "Hyperfine structure of the 2p 2PI 2 state in 9Be+". In: *Physical Review a* 31.4, pp. 2711–2714.

Boyd, G. D. and D. A. Kleinman (1968). "Parametric interaction of focused Gaussian light beams". In: *Journal of Applied Physics* 39.8, pp. 3597–3639. ISSN: 00218979. DOI: 10.1063/1.1656831.

Canetti, L., M. Drewes, and M. Shaposhnikov (2012). "Matter and antimatter in the universe". In: *New Journal of Physics* 14. ISSN: 13672630. DOI: 10.1088/1367-2630/14/9/095012. arXiv: 1204.4186.

Chamberlain, O., E. Segrè, C. Wiegand, and T. Ypsilantis (1955). "Observation of antiprotons [13]". In: *Physical Review* 100.3, pp. 947–950. ISSN: 0031899X. DOI: 10.1103/PhysRev.100.947.

Cohen-Tannoudji, C. (1992). "Atomic Motion in Laser Light". In: *Les Houches, Session LIII, 1990*. Elsevier Science Publisher B.V.

Cozijn, F. M. J., J. Biesheuvel, A. S. Flores, W. Ubachs, G. Blume, A. Wicht, K. Paschke, G. Erbert, and J. C. J. Koelemeij (2013). "Laser cooling of beryllium ions using a frequency-doubled 626 nm diode laser". In: *Optics Letters* 38.13, p. 2370. ISSN: 0146-9592. DOI: 10.1364/ol.38.002370.

Dehmelt, H. G. (1969). "Radiofrequency spectroscopy of stored ions II: spectroscopy". In: *Advances in Atomic and Molecular Physics*. 5th ed. Elsevier, pp. 109–154.

Dine, M. and A. Kusenko (2004). "Origin of the matter-antimatter asymmetry". In: 76.January, pp. 1–30.

Dirac, P. A. M. (1928). "The quantum theory of the electron". In: *Proceedings of the Royal Society of London. Series A, Containing Papers of a Mathematical and Physical Character* 117.778, pp. 610–624. ISSN: 0950-1207. DOI: 10.1098/rspa.1928.0023.

Eades, J. and F. J. Hartmann (1999). "Forty years of antiprotons". In: *Reviews of Modern Physics* 71.1, pp. 373–419. ISSN: 00346861. DOI: 10.1103/revmodphys.71.373.

Folman, R., P. Krüger, J. Schmiedmayer, J. Denschlag, and C. Henkel (2002). "Microscopic atom optics: From wires to an atom chip". In: *Advances in Atomic, Molecular and Optical Physics* 48.C, pp. 263–356. ISSN: 1049250X. DOI: 10.1016/S1049-250X(02)80011-8. arXiv: 0805.2613.

Franken, P. A., A. E. Hill, C. W. Peters, and G. Weinreich (1961). "Generation of optical harmonics". In: *Physical Review Letters* 7.4, pp. 118–119. ISSN: 00319007. DOI: 10.1103/PhysRevLett.7.118.

Freegarde, T., J. Coutts, J. Walz, D. Leibfried, and T. W. Hänsch (1997). "General analysis of type I second-harmonic generation with elliptical Gaussian beams". In: *J. Opt. Soc. Am. B* 14.8, pp. 2010–2016. DOI: 10.1364/JOSAB.14.002010. URL: http://josab.osa.org/abstract.cfm?URI=josab-14-8-2010.

Gabrielse, G., A. Khabbaz, D. S. Hall, C. Heimann, H. Kalinowsky, and W. Jhe (1999). "Precision mass spectroscopy of the antiproton and proton using simultaneously trapped particles". In: *Physical Review Letters* 82.16, pp. 3198–3201. ISSN: 10797114. DOI: 10.1103/PhysRevLett.82.3198.

Groot-Berning, K., T. Kornher, G. Jacob, F. Stopp, S. T. Dawkins, R. Kolesov, J. Wrachtrup, K. Singer, and F. Schmidt-Kaler (2019). “Deterministic single-ion implantation of rare-earth ions for nanometer-resolution color-center generation”. In: *Physical Review Letters* 123.10, p. 106802. ISSN: 10797114. DOI: 10.1103/PhysRevLett.123.106802. arXiv: 1902.05308. URL: https://doi.org/10.1103/PhysRevLett.123.106802.

Hannig, S., J. Mielke, J. A. Fenske, M. Misera, N. Beev, C. Ospelkaus, and P. O. Schmidt (2018). “A highly stable monolithic enhancement cavity for second harmonic generation in the ultraviolet”. In: *Review of Scientific Instruments* 89.1. ISSN: 10897623. DOI: 10.1063/1.5005515. arXiv: 1709.07188. URL: http://dx.doi.org/10.1063/1.5005515.

Hansch, T. W. and B. Couillaud (1980). “Laser frequency stabilization by polarization spectroscopy of a reflecting reference cavity”. In: *Optics Communications* 35.3, pp. 441–444. ISSN: 00304018. DOI: 10.1016/0030-4018(80)90069-3.

Hänsch, T. W. and A. L. Schawlow (1975). “Coolong of Gases by Laser Radiation”. In: *Optics Communications* 13.I, pp. 68–69.

Heinrich, J. (2018). “A Be+ Ion Trap for H2+ Spectroscopy”. PhD thesis. URL: https://tel.archives-ouvertes.fr/tel-01889833.

Jacob, G. (2016). “Ion Implantation and Transmission Microscopy with Nanometer Resolution Using a Deterministic Ion Source Dissertation”. In:

Jacob, G., K. Groot-Berning, S. Wolf, S. Ulm, L. Couturier, S. T. Dawkins, U. G. Poschinger, F. Schmidt-Kaler, and K. Singer (2016). “Transmission Microscopy with Nanometer Resolution Using a Deterministic Single Ion Source”. In: *Physical Review Letters* 117.4, pp. 1–6. ISSN: 10797114. DOI: 10.1103/PhysRevLett.117.043001.

Kaushal, V., B. Lekitsch, A. Stahl, J. Hilder, D. Pijn, C. Schmiegelow, A. Bermudez, M. Müller, F. Schmidt-Kaler, and U. Poschinger (2019). “Shuttling-Based Trapped-Ion Quantum Information Processing”. In: pp. 1–23. arXiv: 1912.04712. URL: http://arxiv.org/abs/1912.04712.

Kielpinski, D., B. E. King, C. J. Myatt, C. A. Sackett, Q. A. Turchette, W. M. Itano, C. Monroe, D. J. Wineland, and W. Zurek (2000). “Sympathetic cooling of trapped ions for quantum logic”. In: *Physical Review A* 61.3, p. 032310. ISSN: 10941622. DOI: 10.1103/PhysRevA.61.032310. URL: http://link.aps.org/doi/10.1103/PhysRevA.61.032310%7B%5C%%7D5Cnhttp://pra.aps.org/abstract/PRA/v61/i3/e032310%7B%5C%%7D5Cnhttp://pra.aps.org/pdf/PRA/v61/i3/e032310.

Koelemeij, J. C., W. Hogervorst, and W. Vassen (2005). “High-power frequency-stabilized laser for laser cooling of metastable helium at 389 nm”. In: *Review of Scientific Instruments* 76.3. ISSN: 00346748. DOI: 10.1063/1.1865752.

Leefer, N., K. Krimmel, W. Bertsche, D. Budker, J. Fajans, R. Folman, H. Häffner, and F. Schmidt-Kaler (2017). “Investigation of two-frequency Paul traps for antihydrogen production”. In: *Hyperfine Interactions* 238.1. ISSN: 15729540. DOI: 10.1007/s10751-016-1388-0. arXiv: 1603.09444.

Major, F., V. N. Gheorghe, and G. Werth (2005). *Charged Particle Traps*. Springer Berlin Heidelberg.

Nörtershäuser, W. et al. (2015). “Precision Test of Many-Body QED in the Be+ 2p Fine Structure Doublet Using Short-Lived Isotopes”. In: *Physical Review Letters* 115.3, pp. 2–6. ISSN: 10797114. DOI: 10.1103/PhysRevLett.115.033002.

Paul, W., H. P. Reinhard, and U. von Zahn (1958). “Das elektrische Massenfilter als Massenspektrometer und Isotopentrenner”. In: *Zeitschrift für Physik* 152.2, pp. 143–182. ISSN: 14346001. DOI: 10.1007/BF01327353.

Paul, W. (1990). “Electromagnetic Traps for Charged and Neutral Particles”. In: *Reviews of Modern Physics* 62, p. 531. ISSN: 15213773. DOI: 10.1002/anie.199007391.

Pérez, P. (2011). “Proposal to measure the Gravitational Behaviour of Antihydrogen at Rest The GBAR Collaboration Contact person : List of Authors”. In: p. 108.

Poulsen, O., T. Andersen, and N. J. Skouboe (1975). “Fast-beam, zero-field level-crossing measurements of radiative lifetimes, fine and hyperfine structures in excited states of ionic and neutral beryllium”. In: *Journal of Physics B: Atomic and Molecular Physics* 8.9, pp. 1393–1405. ISSN: 00223700. DOI: 10.1088/0022-3700/8/9/006.

Rothe, S., B. A. Marsh, C. Mattolat, V. N. Fedosseev, and K. Wendt (2011). “A complementary laser system for ISOLDE RILIS”. In: *Journal of Physics: Conference Series* 312.SECTION 5, pp. 1–6. ISSN: 17426596. DOI: 10.1088/1742-6596/312/5/052020.

Ruster, T., C. Warschburger, H. Kaufmann, C. T. Schmiegelow, A. Walther, M. Hettrich, A. Pfister, V. Kaushal, F. Schmidt-Kaler, and U. G. Poschinger (2014). “Experimental realization of fast ion separation in segmented Paul traps”. In: *Physical Review A - Atomic, Molecular, and Optical Physics* 90.3, pp. 1–10. ISSN: 10941622. DOI: 10.1103/PhysRevA.90.033410. arXiv: 1405.5046.

Sansonetti, J. E. and W. C. Martin (2005). “Handbook of basic atomic spectroscopic data”. In: *Journal of Physical and Chemical Reference Data* 34.4, pp. 1559–2259. ISSN: 00472689. DOI: 10.1063/1.1800011.

Setija, I. D., H. G. Werij, O. J. Luiten, M. W. Reynolds, T. W. Hijmans, and J. T. Walraven (1993). “Optical cooling of atomic hydrogen in a magnetic trap”. In: *Physical Review Letters* 70.15, pp. 2257–2260. ISSN: 00319007. DOI: 10.1103/PhysRevLett.70.2257.

Smorra, C. et al. (2017). “A parts-per-billion measurement of the antiproton magnetic moment”. In: *Nature* 550.7676, pp. 371–374. ISSN: 14764687. DOI: 10.1038/nature24048.

Walz, J. and T. W. Hänsch (2004). “A proposal to measure antimatter gravity using ultracold antihydrogen atoms”. In: *General Relativity and Gravitation* 36.3, pp. 561–570. ISSN: 00017701. DOI: 10.1023/B:GERG.0000010730.93408.87.

Wilson, A. C., C. Ospelkaus, A. P. Van Devender, J. A. Mlynek, K. R. Brown, D. Leibfried, and D. J. Wineland (2011). “A 750-mW, continuous-wave, solid-state laser source at 313 nm for cooling and manipulating trapped 9Be + ions”. In: *Applied Physics B: Lasers and Optics* 105.4, pp. 741–748. ISSN: 09462171. DOI: 10.1007/s00340-011-4771-1.

Wineland, D. J., R. E. Drullinger, and F. L. Walls (1978). “Radiation-pressure cooling of bound resonant absorbers”. In: *Physical Review Letters* 40.25, pp. 1639–1642. ISSN: 00319007. DOI: 10.1103/PhysRevLett.40.1639.

Wolf, S. (2019). “Ion Crystals for Fundamental Research on Matter-Antimatter Symmetry and on Photon Statistics”. PhD thesis.

Wolf, S., D. Studer, K. Wendt, and F. Schmidt-Kaler (2018). “Efficient and robust photo-ionization loading of beryllium ions”. In: *Applied Physics B: Lasers and Optics* 124.2, pp. 1–6. ISSN: 09462171. DOI: 10.1007/s00340-018-6903-3. URL: http://dx.doi.org/10.1007/s00340-018-6903-3.

Wübbena, J. B., S. Amairi, O. Mandel, and P. O. Schmidt (2012). “Sympathetic cooling of mixed-species two-ion crystals for precision spectroscopy”. In: *Physical Review A - Atomic, Molecular, and Optical Physics* 85.4, pp. 1–14. ISSN: 10502947. DOI: 10.1103/PhysRevA.85.043412. arXiv: 1202.2730.

Wuerker, R. F., H. Shelton, and R. V. Langmuir (1959). “Electrodynamic containment of charged particles”. In: *Journal of Applied Physics* 30.3, pp. 342–349. ISSN: 00218979. DOI: 10.1063/1.1735165.

Yi, J., C. Geppert, R. Horn, and K. Wendt (2003). “Temporal Control of Pulses from a High-Repetition-Rate Tunable Ti:Sapphire Laser by Active Q-switching”. In: *Japanese Journal of Applied Physics* 42.Part 1, No. 8, pp. 5066–5070.

DOI: 10.1143/jjap.42.5066. URL: https://doi.org/10.1143%7B%5C%%7D2Fjjap.42.5066.